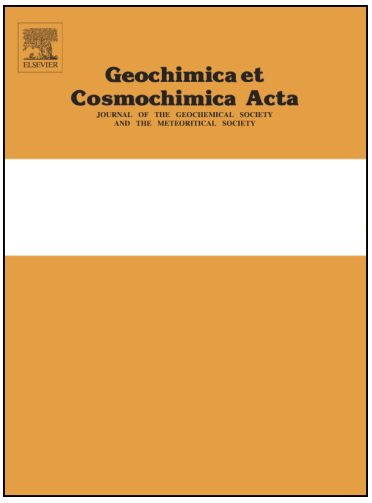

Kinetic D/H fractionation during hydration and dehydration of silicate glasses, melts and nominally anhydrous minerals

M. Roskosz, E. Deloule, J. Ingrin, C. Depecker, D. Laporte, S. Merkel, L. Remusat, H. Leroux

PII: S0016-7037(18)30245-X
DOI: https://doi.org/10.1016/j.gca.2018.04.027
Reference: GCA 10748

To appear in: *Geochimica et Cosmochimica Acta*

Received Date: 12 September 2017
Accepted Date: 27 April 2018

Please cite this article as: Roskosz, M., Deloule, E., Ingrin, J., Depecker, C., Laporte, D., Merkel, S., Remusat, L., Leroux, H., Kinetic D/H fractionation during hydration and dehydration of silicate glasses, melts and nominally anhydrous minerals, *Geochimica et Cosmochimica Acta* (2018), doi: https://doi.org/10.1016/j.gca.2018.04.027

Kinetic D/H fractionation during hydration and dehydration of silicate glasses, melts and nominally anhydrous minerals

M. Roskosz[1, 2*], E. Deloule[3], J. Ingrin[2], C. Depecker[2], D. Laporte[4], S. Merkel[2], L. Remusat[1] and H. Leroux[2]

1 Muséum National d'Histoire Naturelle, Sorbonne Université, UMR CNRS 7590, IRD, Institut de Minéralogie, de Physique des Matériaux et de Cosmochimie, 75005 Paris, France

2 Unité Matériaux et Transformations, Université Lille 1, CNRS UMR 8207, Bâtiment C6, 59655 Villeneuve d'Ascq, France

3 CRPG, CNRS, Université de Lorraine, UMR 7358, Vandoeuvre les Nancy, F-54501, France

4 Laboratoire Magmas & Volcans, Université Clermont Auvergne - CNRS - IRD, OPGC, 6 Avenue Blaise Pascal, 63178 Aubière Cedex, France.

*Corresponding author: mathieu.roskosz@mnhn.fr

To be submitted to Geochimica et Cosmochimica Acta

Abstract:

The distribution of hydrogen isotopes during diffusion-driven aqueous processes in silicate glasses, melts and crystals was investigated. Hydration/dehydration experiments were performed on silica glasses at 1000°C and 1 bar total pressure. Dehydration triggered by decompression-driven bubble nucleation and growth was performed on rhyolitic melts at 800°C and a few hundred MPa. Hydrogen extraction from a nominally anhydrous mineral (grossular) single crystal was carried out at 800°C and ambient pressure. After these three series of experiments, pronounced water (*sensu lato)* concentration profiles were observed in all recovered samples. In the grossular single-crystal, a large spatial variation in H isotopes (δD variation > 550‰) was measured across the sample. This isotopic distribution correlates with the hydrogen extraction profile. The fit to the data suggests an extreme decoupling between hydrogen and deuterium diffusion coefficients (D_H and D_D respectively), akin to the decoupling expected in a dilute ideal gas ($D_H/D_D \approx 1.41$). Conversely, no measurable spatially- and time-resolved isotopic variations were measured in silicate glasses and melts. This contrasted behavior of hydrogen isotopes likely stands in the different water speciation and solution mechanisms in the three different materials. Glasses and melts contain essentially hydroxyl and molecular water groups but the mobile species is molecular water in both cases. Protonated defects make up most of the water accommodated in grossular and other nominally anhydrous minerals (NAM). These defects are also the mobile species that diffuse against polarons. These results are crucial to accurately model the degassing behavior of terrestrial and lunar magmas and to derive the initial D/H of water trapped in fluid inclusions commonly analyzed in mantle NAMs, which suffered complex geological histories.

1. Introduction:

Water is one of the most ubiquitous volatile compounds in the solar system. It is found in primitive meteorites, it is detected in Earth-like planetary bodies including Mars and the Moon, and it makes up the surface of a number of asteroids. Water in these rocks has been preserved over time even when intense thermal processing of the planetary materials occurred. Water chemically reacts with silicates and oxides to form protonated point defects forming OH-bonds or strongly bound molecular water layers deeply stabilized in the silicate structure. However, despite the common occurrence of hydrous phases in planetary materials, the origin of water, its budget and timing of delivery are not fully understood. In particular, the formation and persistence of hydrous silicate dusts within the protoplanetary disk is very controversial (Prinn & Fegley, 1989; Bose & Ganguly, 1995; Drake, 2005). The budget and the carrier of the water delivered to planets is also debated (e.g. Lunine et al., 2003; Albarède, 2009; Hartogh et al., 2011; Sarafian et al., 2014; Hallis et al., 2015; Altwegg et al., 2015; Hauri et al., 2015; Barnes et al., 2016). Clues to understanding the origin of water lie essentially in its hydrogen isotopic composition. However, interpretations of this powerful proxy can remain biased because these isotope variations do not only probe geochemical reservoirs. Chemical reactions driven by thermodynamic equilibrium and disequilibrium processes also affect the isotopic signature of silicate materials. Therefore to provide a reliable interpretation of the D/H ratios measured in these different materials (i.e. to make mass balance calculation or to model degassing), the assessment of equilibrium/kinetic isotope fractionation is critical.

In the past decades, a large body of literature has been devoted to the determination of equilibrium fractionation factors of coexisting H-bearing phases in gas, liquid and solid. Conversely, little is known on the effect of disequilibrium and kinetically-controlled reactions. First order modeling of degassing, assuming an ideal behavior for dissolved water molecules (*sensu lato*, including protons, OH and H_2O groups) is commonly carried out and provides an upper limit to the magnitude of kinetic fractionation (e.g. Tartèse et al., 2013; Barnes et al., 2016). Yet no experimental quantifications are available to disentangle reservoir, equilibrium and partial disequilibrium effects except on a few hydrous minerals (e.g. Pilorgé et al., 2017).

In this experimental work, we investigate the isotopic consequences of partial hydration/dehydration/degassing of silicates. Experimental conditions and materials were selected to mimic different processes at play in various rock-forming environments. Firstly, the hydration/dehydration of a silica glass in contact with water vapor was performed to document the possible interactions between vapor and the amorphous silicate components detected in most of primitive planetary disks and repeatedly observed in the matrix of well preserved chondrites (Abreu and Brearley, 2010). Although silica is a very simplified analogue, it is an excellent proxy because the speciation of water and its dynamics have been extensively studied (e.g. Doremus, 1995; Davis and Tomozawa, 1996; Davis et al., 1995; Behrens, 2010). Secondly, magma degassing was modeled by the controlled decompression of a presaturated rhyolitic melt, leading to diffusion-controlled nucleation and growth of H_2O bubbles within the melt. Thirdly, the isotopic effect of the loss of water stored in nominally anhydrous minerals (NAMs) was studied by high temperature, ambient pressure, hydrogen extraction experiments in a single grossular crystal. With these results in hand, the relationships between water speciation and isotopic effects are discussed and the parameters required to quantitatively account for the kinetic fractionation of hydrogen isotopes are provided.

2. Experimental and analytical methods

2.1. Sample preparation

2.1.1. Silica glass

Silica samples were prepared from Infrasil 301 and Herasil 102 (Heraeus Co.) for hydration and dehydration experiments, respectively. The nominal water content of Infrasil 301 is less than 8 ppm whereas Herasil contains less than 150 ppm. In both cases, the parent rods (1 cm in diameter) were cut as disks (approximately 1-2 mm thick) in ethanol and double-sided polished to an optical quality (using SiC papers and 1/4μm diamond suspension on polishing clothes and ethanol as the polishing fluid). Annealing was performed in a tubular furnace (Nabertherm Co.) at the university of Lille (UMET) at 1000°C (±3°C). Run durations extended to 30 days. Water was introduced into the furnace as vapor. It was generated by bubbling pure Ar in a large volume (500 mL) of ultrapure (Milli-Q) water at 20°C (±1°C) before injection into the tubular furnace. In these conditions, the f_{H2O} was close to 20×10^{-3} bar (the saturation pressure at 1 bar total pressure and 20°C). Presaturation of the alumina tube was performed during a week before running the experiments. The experimental setup was designed to limit the causes of hydrogen isotope fractionation to the vapor production and potentially to its adsorption on the sample. In this respect, we note that at 20°C, the vapor should be lighter than the liquid reservoir by about 81‰ (Horita and Wesolowski, 1994). Furthermore, the negligible amount of water vaporized at 20°C during the runs implies that the isotopic composition of the liquid reservoir (and so the vapor reservoir) can be considered as constant over the entire duration of experiments. After quench, samples were sliced perpendicular to the surface of disks (slices were 131, 165 and 186 μm in thickness for the sample annealed for 3, 8 and 30 days respectively). Again, samples were polished to optical quality without water and stored in a glovebox under inert atmosphere (Ar) before analyses of profiles by FTIR and SIMS. Dehydration experiments were performed in the same furnace but without injection of water vapor. Only dry argon flowed during the experiments. The furnace was heated to 1600°C for 2 days before the run in order to extract as much water as possible from the alumina tube. The thicknesses of the samples analyzed by FTIR were 193 and 147 μm in thickness for the reference and the sample annealed for 3 hours, respectively.

2.1.2. Rhyolitic melts

The rhyolitic samples were described in a previous study (Mourtada-Bonnefoi and Laporte, 2004). The starting material was an obsidian from Güney Dagi, Turkey (76.51% SiO_2, 12.56% Al_2O_3, 0.70% FeO, 0.01% MgO, 0.25% CaO, 4.47% Na_2O, 4.24% K_2O, 0.03% TiO_2, 0.07% MnO in wt%). Samples were presaturated in water in an internally heated pressure vessel and were isobarically quenched to prevent bubble nucleation at 250 MPa and 1000°C. The saturated glasses initially contained about 6.6 ± 0.2 wt% H_2O as determined by FTIR (Hamada et al., 2010). Glass cylinders were prepared from this starting material and welded in a new platinum capsule (with no water added). The capsule was placed in an externally heated pressure vessel fitted with a rapid quench extension. It was first cold-pressurized to 230-240 MPa and then heated to 800°C in 60-90 min. Oxygen fugacity was not buffered during the decompression experiments, but was assumed to remain close to the Ni-NiO buffer (as in the saturation experiments) because of the short run durations involved. All experiments began by a 15 min relaxation stage at 260 MPa, 800°C. Pressure was then decreased at a rate equal to 27.8 or 167 kPa.s^{-1} down to a final value P_f ranging from 119 to 59 MPa. As soon as pressure P_f was reached, the experiment was quenched isobarically at an initial rate of 200°C.s^{-1}. We focused on two samples decompressed at 27.8 kPa.s^{-1} (samples C20 and C19 quenched at P_f =88.6 and 85.1 MPa, respectively; Mourtada-Bonnefoi and Laporte, 2004), and one sample decompressed at 167 kPa.s^{-1} (sample B14 quenched at P_f =70.7 MPa). In these three experiments, the homogeneous bubble nucleation occurred at 90 ± 2 MPa, and yielded a core with a relatively small number of large bubbles: about 10 bubbles per mm^3 in the experiments at 27.8 kPa.s^{-1}, with a mean diameter of 77 μm (C20) to 187 μm (C19); 350 bubbles per mm^3 in the experiment at 167 kPa.s^{-1}, with a mean diameter equal to 77 μm (B14). The SIMS analyses were performed in the cores of these three samples.

2.1.3. Grossular crystal

Grossular ($Ca_3Al_2Si_3O_{12}$) is known to incorporate greater concentrations of hydrogen than any other natural member of the garnet group. The single crystal studied (38.16% SiO_2, 16.15% Al_2O_3, 1.11% FeO, 7.45% Fe_2O_3, 0.24% MgO, 34.93% CaO, 0.02% Na_2O, 0.42% TiO_2,

0.43% MnO in wt%) originate from a vesuvianite-bearing fissure in a relatively large rodingite body (approximate dimension 10 m x 2 m x 5 m), located in the serpentinite massif of Rotkopf in the Zillertaler Alps, Austria. Some parts of the material were without fractures, free of inclusions of other minerals, and of gem quality. A double-sided polished parallelepiped sample (4740x2890x1140 µm) was annealed in dry air, at 800°C (±5°C) and at ambient pressure to extract hydrogen. The mechanisms involved in this dehydration are discussed below. A high-temperature furnace equipped with a horizontal alumina tube was used for this purpose. After the extraction experiment, a slice was cut from the central part perpendicular to the larger thickness of the annealed sample and polished on both sides (591x2890x1140 µm; see detail of the method in Ingrin and Blanchard 2006). The SIMS analyses (D/H and water content) were performed across the sample approximately perpendicular to the initial free surface of the sample. In addition, an infrared absorption profile was then measured along the SIMS profile.

2.2. Analytical protocols

2.2.1. Fourier-transform Infrared Spectroscopy

Fourier-transform Infrared Spectroscopy (FTIR) analyses were performed on two different instruments (LASIR, Université Lille 1). For silica samples, the FTIR absorbance spectra were recorded by a Perkin Elmer FTIR Spotlight 300 equipped with the FPA technology (Focal Plan Area) and a MCT (Mercury Cadmium Telluride) detector. Spectra were recorded in the range of wave number from 700 cm^{-1} to 5000 cm^{-1} with a spectral resolution of 4 cm^{-1} and 32 scans. They were recorded in point mode with a step of 10 µm and a slit of 10x100 $µm^2$. This geometry was chosen to improve the signal without modifying the depth spatial resolution (the length of the samples was 5 to 10 times longer than their thickness).

Turning to the grossular crystal, the OH diffusion profiles were analyzed with a Bruker Hyperion 3000 FTIR-microscope coupled to a Bruker Vertex 70 spectrometer equipped with a liquid-N_2-cooled MCT detector in the laboratory of Infrared and Raman Spectrochemistry. The whole system was continuously purged with dry air to minimize atmospheric contamination. The sample was placed on a 2 mm thick CaF_2 disc. The infrared beam was focused on the surface of the doubly polished samples with a cassegrainian objective (15x

for a spot of 60 x 60 µm and 36x for a spot of 30 x 30 µm). A profile was measured across the whole sample with the larger spot size (60 x 60 µm every 40 µm) while a shorter profile was measured with the smaller spot size (30 x 30 µm every 30 µm). Measurements were also tested in focusing the beam into the middle of the 951 µm thick sample. No major difference was observed. A total of 256 scans were accumulated with a resolution of 4 cm^{-1} for each measurement. The background spectrum was measured before the profile measurement on the CaF_2 disc.

2.2.2. Secondary Ion Mass Spectrometry

The D/H were acquired using the Cameca IMS 1270 and IMS 1280 ion probes at CRPG-CNRS-Nancy during 3 sessions. An additional session using the Cameca IMS 7f at the Institut Jean Lamour (Nancy) was dedicated to the measurement of the SiH/Si close to the bubbles formed in the decompressed rhyolitic melts. In order to minimize surface hydrogen contamination, the D/H and H_2O concentrations were measured on standards and samples dried for 48h at 70°C before gold coating and then stored several hours before analysis in the SIMS storage chamber under ultra-high vacuum (2-3$\times 10^{-8}$ torr).

On the IMS 7f, a 10 nA O^- primary ion beam was focused on a 20 µm diameter spot. The ^{30}Si and ^{29}SiH secondary ions were measured with a mass resolution of 3000. The SiH/Si were then considered as representative of the water content in the sample. No standards were used during this session. The absolute measured values of this ratio are therefore certainly affected by matrix effects and cannot be taken as face values. Therefore, we only consider in the following the relative variations of the SiH^+/Si^+ ratio along concentration profiles close to the bubbles and from a sample to another.

Isotope ratios and water concentrations were determined on both IMS 1270 and 1280. During the first session, a 6 nA O^- primary ion beam was focused on a 10 µm diameter spot. The H^+ and D^+ secondary ions were measured with a mass resolution of 2000, by peak switching in monocollection mode and EM ion counting (H^+ for 4 s, D^+ for 20 s, and background for 4 s at mass 0.98). During the second and third sessions, a 2 nA Cs^+ primary ion beam was focused on a 10 µm diameter area. The electron gun was used for charge compensation. The EGUN emission was adjusted to limit the H^- emission below 1000 cps with the primary beam off. The H^- and D^- secondary ions were measured with a high mass

resolution of 2000, by peak switching in monocollection mode (H^- on FC for 4 s, D^- on EM for 20 s and background for 4 s at mass 0.98 for FC and for 4 s at the mass 1.98 for EM). For each measurement, the sample was pre-sputtered for 2 minutes. The beam position relative to the field aperture and the magnetic field were checked automatically and 20 to 24 cycles acquired. The D/H instrumental fractionation and the H useful yield were determined by using the MPI DING reference glasses (Jochum et al., 2006). Finally, during the third session, the water content was also investigated by measuring the OH^-/O^- and OH^-/Si^- ratios. Measurements were made with the same primary Cs^+ beam and EGUN setting as in the second session. The negative secondary ions were collected by peak switching in monocollection mode at a mass resolution of 7000 to ensure the full separation of ^{17}O and ^{16}OH. The acquisition cycles included ^{16}O on FC, ^{17}O and ^{16}OH on EM, ^{28}Si on FC and ^{30}Si on EM. The FC and EM backgrounds were measured at the masses 15.8 and 16.8 respectively. For each measurement, the sample was pre-sputtered for 2 minutes, the beam position and the magnetic field were checked automatically and 12 cycles were acquired.

All isotopic data collected were internally standardized. Data collected on silica samples are expressed as the deviation (δD in ‰) from the isotopic compositions of the starting materials measured during the same analytical session. Data collected on rhyolite glasses are expressed as the deviation (δD in ‰) from the isotopic compositions measured on the same samples at long distances from bubbles (>200 μm), where the water content was found identical to the initial water content (see below). In both cases, several analyses (n=4-10) were performed and did not reveal measurable variations of the starting isotopic composition of these glasses. Data collected on the grossular crystal were processed in a more advanced way, fully described in the result section. Data are presented as the deviation (δD in ‰) from the mean composition of the inner part of the sample, where FTIR and SIMS data suggest no significant water loss (see below for details). The δD notations in this article are therefore not expressed relative to VSMOW (Vienna Standard Mean Ocean Water) with the notable exception of Fig. 5b (see below for more details). This study thus describes the amplitude of the fractionation produced by partial hydration/dehydration of planetary materials and does not attempt to reproduce quantitatively the absolute D/H values measured on natural samples.

3. Results

3.1. Hydration of silica glass during vapor/solid interactions

Water uptake during gas-glass interaction at 1000°C only affects a few hundreds of microns below the sample surface (Table 1, Fig. 1a). The speciation of water in our samples is unambiguously dominated by hydroxyl groups as repeatedly observed in similar glasses hydrated at temperatures above 700°C (Davis and Tomozawa, 1996; Behrens 2010). For this reason, OH quantification was performed by considering the extinction coefficient provided by Davis et al. (1996) for the OH band at 3673 cm^{-1}. At the gas-glass interface, the OH concentration is close to the equilibrium water solubility predicted from literature data extrapolated to 1000°C and to a vapor pressure of $20x10^{-3}$ bar (Moulson and Roberts, 1960). The measured concentrations (134 ± 4 ppm) are in excellent agreement with predictions (~124 ppm) for long run experiments (8 and 30 days). Conversely, the concentration measured at the surface of the sample annealed for 3 days (~160 ppm) is slightly higher than the equilibrium value. The reason for this slight overshoot is unclear but a time-dependent variability of the surface water concentration has been reported for silica glasses and was attributed to the competing effects of structural relaxation and water diffusion (Tomozawa and Davis, 1999).

Another typical feature of such hydration experiments on silica glass is that the diffusion coefficient of water is a strong function of the water content. It increases with the water content as depolymerization of the silica network proceeds (e.g. Doremus, 1995; Behrens, 2010). A direct consequence is that concentration profiles present an unusual shape with a water-saturated rim at the surface, which grows over time and is followed, in depth, by an abrupt drop (Fig. 1a). In this context, a constant diffusion coefficient cannot be used for long-run experiments (e.g. Behrens, 2010). The primary goal of our study is not to provide a determination of the concentration-dependence of the water diffusion coefficient in our samples. As a consequence, we did not model our dataset with such concentration-dependence. We note however that it can be satisfactorily modeled with $D_{H2O} = 10^{-14}$ $m^2.s^{-1}$, which is a reasonable average value for our experimental conditions (Moulson and Roberts, 1961; Behrens, 2010).

Finally, turning to the isotopic composition of the water dissolved in these silica samples, the dataset clearly points to an absence of detectable and systematic variation at

the level of ~20-30‰ (1s.d.). This holds true for all analyzed samples (Table 2, Fig. 1b). Therefore our results suggest that no measurable diffusion-driven fractionation affects the D/H signature of water during the hydration of silicate glasses at high temperature.

3.2. Dehydration of silica glass during vapor/solid interactions

Dehydration of OH-bearing silica glass does not proceed by the exact reverse reaction as hydration experiments (Moulson and Roberts, 1961). After only 3 hours at 1000°C, the bulk sample has uniformly lost a large fraction of the initial water content (Table 1, Fig. 2a). Hence, dehydration occurs within a much shorter timescale than hydration of initially anhydrous silica glass samples. This result combined to the very limited extent of the concentration gradient at the vapor-solid interface suggests that dehydration is limited by water surface desorption and not by its bulk outward diffusion.

Turning to the isotopic composition of the remaining water dissolved in the sample after the experiment, analytical results show a potentially small constant difference (δD =-23$\pm$22 ‰ at 1sd) across the sample relative to the starting material (Table 2, Fig. 2b). This deviation is not significant and the isotopic composition of the dehydrated sample is taken as homogeneous at the level of ~20-30 ‰ (1 s.d.). As discussed below, any kinetic process would let the solid residue preferentially enriched in the heavy isotope (deuterium). The small difference measured here is opposite.

3.3. Rhyolitic magma degassing during decompression

During the decompression of the melt, the water content of the molten silicate is assumed to be minimum close to the bubbles and to increase with increasing distance from the bubbles as a result of diffusive bubble growth. For each sample selected for this study, microprobe analyses of the glass were previously made as far as possible from the bubbles visible in the polished section (Mourtada-Bonnefoi and Laporte, 2004). These previous results provide strong arguments for disequilibrium degassing since the water contents are similar to the initial water content: about 6.6 wt% and much higher than the equilibrium values, at P_f, of 3.9 - 3.4 wt% (Zhang, 1999; Tamic et al., 2001). The SiH/Si measured in this study by IMS 7f confirms and extends previous conclusions. Firstly, the SiH/Si signal is

constant and almost identical for all samples at distances as close as 200 microns from the bubbles (Table 3, Fig. 3a), and decreases closer to the bubbles. Secondly, for the sample with the largest bubbles (sample C19 decompressed at 27.8 kPa.s^{-1} and quenched at P_f = 85.1 MPa), the SiH/Si at the interface with the bubble drops down to 60% (extrapolated from available data) of the initial signal. If the measured ratios are proportional to the water content in the concentration range of interest (from 7 to 3 wt%), then it is possible to estimate the water content at the interface to be about 4 wt%. This value is close to the water solubility at equilibrium (Zhang, 1999; Tamic et al., 2001). For the two other samples, exhibiting smaller bubbles, the water content at the interface is higher than the equilibrium values (3.8-3.9 wt% at P_f = 88.6 MPa and 3.4-3.5 wt% at P_f = 70.7 MPa): about 6 wt% in sample C20 decompressed at 27.8 kPa.s^{-1} and quenched just below the nucleation pressure (P_f = 88.6 MPa); about 5.6 wt% in sample B14 decompressed at 167 kPa.s^{-1} and quenched at P_f = 70.7 MPa. Therefore, for all samples disequilibrium degassing occurred during decompression.

Turning to the isotopic composition of the water dissolved in the rhyolitic glass close to the bubbles, the results clearly point to a lack of detectable variation at the level of 20‰ (1s.d.). This holds true for all analyzed areas and for the three samples (Table 3, Fig. 3b). The decompression rate and the final pressure have no effect on the D/H of the remaining water. Here again, our results suggest that no significant diffusion-driven fractionation affects the D/H signature of water during magma degassing.

3.4. Grossular dehydration

Based on the position of the main OH bands Rossman and Aines (1991) identified seven different classes of FTIR spectrum in natural grossular. This grossular belongs to class 5 spectra. It means that they are dominated by a band at 3611 cm^{-1} and two side bands at about 3664 cm^{-1} and 3562 cm^{-1}. This grossular is a typical single crystal from cavities in meta-rodingites found in alpine type serpentinites. The integrated absorbance in the region 3700–3400 cm^{-1} was determined to calculate the OH content of the samples (Fig.4). The absorption coefficient proposed by Rossman and Aines (1991) was used. This grossular crystal initially contained 0.14 (± 0.03) wt% H_2O and the OH content was homogenous within experimental and statistical errors. It is of note that the correct absorption coefficients for

garnets have been a matter of debate (Maldener et al. 2003), but it is of minor consequence here as we only need information on the relative variation of the OH-content during experiments.

After annealing in air for 10h at 800°C, the hydrogen extraction is pronounced (Fig. 5a). A large and quasi-symmetric OH concentration profile was measured by FTIR spectroscopy across the sample with two spot sizes (30x30 microns and 60x60 microns). The maximum absorbance measured was then used to normalize the OH contents determined locally. This maximum absorbance was in excellent agreement with the average initial absorbance measured before annealing. Consequently, the crystal can reasonably be considered as a semi-infinite medium, a simplifying assumption for processing the dataset in order to extract diffusion coefficients. These FTIR profiles are also fully consistent with the OH^-/O^- and OH^-/Si^- profiles measured by SIMS (Table 4, Fig. 5a). In details, the FTIR profile collected over spots of 30x30 microns is slightly more pronounced. This discrepancy may result from the more local nature of the analysis. It is therefore possible to derive, from these four separate datasets, a fairly accurate diffusion coefficient describing the hydrogen extraction in these experimental conditions. Within the assumption of a semi-infinite medium, the full profile across the sample can be modeled analytically with the help of the function proposed by Crank (1956):

$$C(x,t) = \frac{4C_0}{\pi} \sum_{n=0}^{\infty} \frac{-1^n}{2n+1} exp\left(\frac{-D(2n+1)^2\pi^2}{4L^2}\right) \cos\frac{(2n+1)\pi x}{2L}, \quad (1)$$

where *C(x,t)* is the local concentration at coordinates *(x,t)*, where the origin is located at the mid-point of the slab, C_0 is the initial homogeneous concentration at t=0, t is time (s) , x is distance (m), D is the diffusion coefficient ($m^2.s^{-1}$) and L is the half-length of the sample (m). In this experiment, the boundary conditions are C=0 for x=-L, L for any t and C=C_0 for $-L<x<L$ at t=0. With this equation in hands, the diffusion coefficient for hydrogen extraction at T = 800°C derived from the four different profiles are very consistent: 4 (±1) x 10^{-13} $m^2.s^{-1}$, 3 (±1) x 10^{-13} $m^2.s^{-1}$, 2.8 (±1.1) x 10^{-13} $m^2.s^{-1}$, 2.7 (±1) x 10^{-13} $m^2.s^{-1}$ for FTIR (30x30), FTIR (60x60), OH^-/O^- and OH^-/Si^- respectively (Fig. 5a).

The isotope distribution within the grossular crystal drastically contrasts with the results collected on glasses and melts. For this nominally anhydrous mineral (NAM) single

crystal, a large isotopic gradient was measured. From the center of the sample to the edges, the measured δD, without standard corrections and calculated against VSMOW varies by more than 550 ‰ (Table 4, Fig. 5b). Such a profile is expected in the case of a diffusion-driven fractionation during hydrogen extraction. Across the central ~600 µm exhibiting a flat profile of water content (FTIR, OH^-/O^- and OH^-/Si^- ratios) and where no D/H redistribution is expected, the raw δD measured (without standardization nor any corrections, but calculated against VSMOW) only varies within a 70‰ range with a typical spot to spot reproducibility of ±30‰ (Fig. 5b). This variation is significant but much lower than the overall measured variation (covering more than 550‰). Moreover, across this inner part of the sample, the measured δD is also reproducible from a session to another. It is independent of the direction of the measurements and shows a continuous trend (Fig. 5b). The reason for this non-flat profile is unclear but may be a geometrical artifact resulting from the cutting and processing of the sample after water extraction experiments. It may also represent the remnant of a continuous variation of the D/H across the single crystal from which the sample was prepared. This artifact marginally affects the quality of the fits and their quantitative analysis (See Appendix).

Nonetheless, we propose a simple linear correction for this artifact. It is based on the fact that after the experiment, no D/H change can be expected where no measurable water extraction profile can be resolved. We therefore used the continuous linear trend measured on the sample to propose an internal correction of the data. We first defined the inner part of the sample by the presence of a flat plateau in the FTIR, OH^-/O^- and OH^-/Si^- ratios for C/C_0>0.95 (Fig. 5a). A linear regression is then applied to the δD dataset (Fig. 5b) and this contribution is subtracted to the entire data set (Fig.5c). We therefore assumed that a continuous drift affected the entire sample and used the linear regression ($\delta D = -377(\pm19)+0.1(\pm0.3)x$) to internally standardize the whole dataset. The consequence of this procedure is to set the inner part of the samples at a δD~0‰ (the δD reported on Fig. 5c are therefore relative to the homogeneous inner part of the sample). Moreover, without additional processing, a quasi-symmetrical isotopic profile is also obtained. This correction does not affect the quantitative analysis and the discussion since the same fits can be adjusted to the raw data as shown in the appendix.

4. Discussion

4.1. Water speciation in silica glass, rhyolitic melt and grossular

The speciation of water in minerals, liquids and melts controls its solubility and its mobility. In this study, the nature of the hydrogen carrier is also pivotal to model our data and propose applications to natural samples. The speciation of water in silicate glasses and melts has been a matter of concern for several decades. It is now widely accepted that both molecular water and hydroxyl groups generally coexist, their relative proportions depending on the silicate composition, temperature, pressure and water partial pressure (e.g. Stolper, 1982; Schmidt et al., 2013; Fanara et al., 2013). The water speciation may also change as melt is quenched into glass (Dingwell and Webb, 1990; Zhang et al., 1995). One notable exception however is the case for silica glasses and melts. In these materials, when the total water content is lower than 0.3 wt% and at temperature higher than 650°C, water is essentially dissolved as hydroxyl groups (Davis and Tomozawa, 1996). The speciation of water in our silica samples is thus dominated by OH groups and the amount of molecular water is negligible. The situation is different for hydrous rhyolites (Zhang et al., 1997; Ihinger et al., 1999; Hui et al., 2008). The proportion of OH groups increases with melting temperature and pressure but decreases as the total amount of water increases. Here, samples were saturated below 1 GPa at 800°C and contained about 7 wt% water. In these conditions, proportions of OH and molecular H_2O are anticipated to be similar (Ihinger et al., 1999). There is therefore a clear expected difference between the speciation of water in silica and in water-saturated rhyolitic samples.

Turning to the water speciation in garnet minerals (and in other NAMs), H_2O molecules are not detected. Instead, hydrogen is bound to an oxygen-atom, forming a hydroxyl bond, which in turns induces local charge excess usually compensated by a cation vacancy or a cation substitution. The dominant incorporation mechanism in grossular is the "hydrogarnet" substitution, where four OH^- molecules are associated with a silicon vacancy, replacing a SiO_4 tetrahedron (Cohen-Addad, 1967). Hydroxyl groups might also be associated with an octahedral (Al^{3+}) vacancy, which would, for instance require 3 OH^- molecules for local charge balance (Geiger et al., 1991). Finally, a mechanism involving titanium has been

suggested (Johnson, 2003) and can possibly occur in titanium-bearing grossular including the crystal used in this study.

4.2. Microscopic mechanisms controlling water diffusion in silica glass, rhyolitic melt and grossular

Microscopic mechanisms are likely at the origin of the contrasted behavior of hydrogen isotopes reported in this work. The three different materials exhibit very different diffusion mechanisms, which in turns probably explains the different isotopic evolutions observed in glasses, melts and crystals. In amorphous silica, it is generally accepted that water diffuses as molecular water (e.g. Doremus, 1995). These molecules eventually react with the glass network to form immobile hydroxyls (or silanol) in favourable sites following a reaction such as:

$$H_2O+SiOSi \leftrightarrow SiOH + HOSi \quad (2)$$

Even below 1000°C, this reaction is fast compared to the OH intrinsic mobility and reaches the local equilibrium with most of the immobile water present as hydroxyl (Doremus, 1969 ; 1994 ; 1995). Our results are also in agreement with pioneering results of Moulson and Roberts (1961) suggesting that water diffusivities are always lower during hydration than during dehydration experiments (Figs. 1 and 2).

The diffusion of water in more complex and geologically relevant melts such as rhyolites, dacites, andesites and basalts has been extensively studied in the past (e.g. Zhang and Ni, 2010). For some of them, it has been suggested that hydroxyl groups may contribute significantly to the diffusive transport of water. This is the case for dacite, possibly basalts (Behrens et al., 2004) and haploandesite when the total amount of dissolved water is low (Ni et al., 2013). In the latter case, the contribution of hydroxyl to the overall water diffusion can be up to 10-20%. Nonetheless, there is no report of such significant contribution of hydroxyl to water diffusion in rhyolitic melts. Therefore, it is reasonable here to assume that the behavior of water during bubble formation in rhyolites during decompression does not differ from its behavior in silica. In both cases, molecular water is the mobile species while OH groups have a much lower mobility (Zhang and Ni, 2010).

Hydrogen extraction from a garnet crystal is a more complicated process because local charge balance must be conserved. One of the fastest mechanisms of hydrogen release in several iron-bearing minerals was identified as the redox reaction:

$$Fe^{3+}+O^{2-}+ 1/2H_2 <-> Fe^{2+}+OH^{-}. \quad (3)$$

This mechanism was ubiquitously proposed for other nominally anhydrous minerals such as diopside (Hercule and Ingrin, 1999; Woods et al. 2000) and olivine (Mackwell and Kohlstedt, 1990). It also likely operates for iron-rich grossular. Now, the possible mechanisms controlling hydrogen migration through the garnet structure is less well understood than for other NAMs. A few studies suggest nonetheless that processes operating for garnets are similar to other NAMs (Blanchard and Ingrin, 2004; Kurka et al., 2005; Zhang et al 2015). In ferromagnesian olivines, hydrogen diffusion is charge compensated either by a fast flux of polarons or by a slower coupling to metal vacancies diffusion (Mackwell and Kohlstedt, 1990; Kohlstedt and Mackwell, 1998). Concerning iron-poor grossulars, Kurka et al. (2005) showed that migration of hydrogen is likely coupled to the slow migration of metal vacancies. Nonetheless, in iron-bearing natural minerals the extraction mechanism likely involves counter-fluxes of polarons (Mackwell and Kohlstedt, 1990; Hercule, 1999; Demouchy and Mackwell, 2003). In other words, the extraction of hydrogen from this mineral may be described as the oriented jump of protons outward the crystal structure and not as the diffusion of free molecular water as for silicate melts and glasses. In minerals with low-iron content (typically lower than 7% in diopside) the diffusion rate of polarons, which is lower than the mobility of hydrogen measured by H-D exchange control the rate of hydrogen extraction (Ingrin and Blanchard 2006). For higher concentration of iron the diffusion of polaron is faster than the diffusion of hydrogen, in this case it is the mobility of hydrogen that controls the extraction (Ingrin and Blanchard 2006). The grossular presently studied contains more than 8 wt% FeO; it is thus likely that the migration of hydrogen during extraction balanced by a counter-flux of polarons is controlled by the mobility of hydrogen. The control of extraction by the mobility of protons in interstitial positions and not water is likely the origin of the contrasted behavior of hydrogen isotopes between glasses and melts and the grossular crystal.

4.3. Modelling diffusion-driven D/H fractionation in glasses, melts and crystals

The same model of D/H fractionation in glasses and melts can be used to explain our experimental data collected on partially hydrated Infrasil 301 preforms (containing initially about 8 ppm water) as well as for decompressed rhyolitic melts. Since the natural abundance of deuterium is very low (0.0156%), the diffusion coefficient derived from these experiments can be taken as the diffusion coefficient of the pure H-bearing mobile species (here H or H_2O). Then, δD profiles are easily modeled provided that the concentration profiles of the corresponding D-bearing molecules can be calculated. We note at this point that this modeling strategy relies on the determination of the effective diffusion coefficient of water in our samples. As this coefficient is sensitive to the local water content, the quantitative modeling of isotopic profiles may be difficult. However, the lack of any measurable isotopic variation along diffusion profiles makes it unnecessary and impossible to quantitatively address this difficulty. As a case study, we focus below on the dataset collected on the silica glass. We assumed a constant diffusion coefficient of $D_{H2O} = 10^{-14}$ $m^2.s^{-1}$, which is a reasonable average value for our experimental conditions (Moulson and Roberts, 1961; Behrens, 2010).

In this framework, the classical empirical relationship relating the ratio of diffusion coefficients of two isotopes to their inverse mass ratio was used (Richter et al., 1999):

$$D_i / D_j = (m_j / m_i)^{\beta}, \quad (4)$$

where D_i and D_j are diffusion coefficients for isotopes *i* and *j*, m_i and m_j are their respective masses and the β-exponent is estimated by adjusting Eq. 4 to the experimental isotopic profiles. This formalism was successfully applied to an increasingly large number of isotopic systems from Li to Fe isotopes in natural samples (e.g. Sio et al., 2013; Oeser et al., 2015; Richter et al., 2016) and experimental charges (e.g. Richter et al. 1999; Roskosz et al., 2006). It was rarely applied to the D-H system (e.g. Saal et al. 2013). So far, no direct experimental study were specifically dedicated to this system, while, as an empirical law, the β-coefficient has to be experimentally (or computationally) determined. In principle, kinetic theory applied to a perfect gas provides an upper limit of 0.5 for the β-value. For condensed matter it is thus expected that β should take values between 0 and 0.5. With Eq. 4 in hands, the D_D and the diffusion profile of deuterated mobile species were derived as a function of β.

As discussed before, molecular water is the dominant mobile species involved in conventional hydration/dehydration reactions in glasses and melts. Nevertheless, molecular hydrogen diffusion also occurs in more exotic environments, namely i) in very reducing conditions, ii) when the hydrogen fugacity (f_{H2}) is high, iii) when radiolysis occurs *in situ*, for instance during ionizing irradiation of silicates. The last process was recently found efficient to separate D and H of water (and hydroxyl) groups dissolved in amorphous and crystalline silicates (Roskosz et al., 2016). For this reason, we provide models describing the spatial redistribution of H and D, in an amorphous silicate, caused by the diffusion of either molecular water or hydrogen atoms (Fig. 6 a and b). If water molecules are the mobile species (diffusion of H_2O and HDO, mass ratio=18/19), the lack of any measurable δD profiles can be explained by any values for β from 0 to 0.5 (Fig. 6 a and b). In other words, β is unconstrained here. More importantly the moderate mass difference between H_2O and HDO makes the diffusion-driven fractionation of H and D very limited (on the order of 30‰). The situation would be different however in environments where the mobility of hydrogen atoms is favored (instead of molecular water). In this case, a significant fractionation would be expected (Fig. 6 a and b). The amplitude of the fractionation for β=0.5 is of several hundreds of ‰. Such a large diffusion-driven fractionation was indeed recently produced experimentally by electron irradiation of hydrous analogues of the dust present in the protoplanetary disk (Roskosz et al., 2016).

The formalism may, in principle, be somewhat different in the case of the grossular single-crystal. The classical theory of the isotopic mass-dependence of diffusion rates in crystalline solids was developed in the late 1950s. A comprehensive review of this theory can be found in Van Orman and Krawczynski (2015). In summary, the amplitude of the diffusion-driven isotope fractionation diminishes in proportion to the degree to which the diffusion process deviates from that of a purely random walk (Schoen, 1958; Tharmalingam and Lidiard, 1959). The basic equation that relates the diffusivities of two isotopes is then (LeClaire, 1966):

$$\left(\frac{Di}{Dj} - 1\right) = f\left(\frac{\omega i}{\omega j} - 1\right), \quad (5)$$

where ωi and ωj represent the frequency of a jump of two isotopes *i* and *j* to an adjacent lattice site (vacancy or interstitial) and *f* is the correlation coefficient. In the simplest case of

a random walk, with no correlation between successive jumps, (i.e. when the motion of the atom during a jump is fully decoupled from the vibrations of the surrounding atoms), f = 1. Furthermore, when there is no such coupling between the vibrations of the jumping atom and of the rest of the crystal, the ratio of jump frequencies of the two isotopes is given by (LeClaire, 1966).

$$\left(\frac{\omega i}{\omega j}\right) = \left(\frac{m_j}{m_i}\right)^{1/2}. \quad (6)$$

Combining Eq. 5 and 6, allow us write Eq. 4 with β=0.5 when f=1. There are often correlations between jumps, and generally, f < 1. Nonetheless, there are a few cases where f is close to unity. Notably, diffusion of a trace element by a simple interstitial mechanism is uncorrelated because all adjacent interstitial sites of the same type are equivalent. For this reason, diffusion-driven isotope fractionation is expected to be large, close to a square root of mass dependence, when an interstitial mechanism is involved.

The diffusion of protons in NAMs likely obeys this description. Though microscopic mechanisms may differ from one mineral to the other and as a function of their chemical composition, diffusion of trace amount of H-defects is always faster than any vacancy in the crystal structure. Hydrogen diffusion is thus essentially interstitial in olivine and other NAMs in general. Therefore, the same procedure as for glasses was applied to the δD profile. The model only considers the mobility of hydrogen and deuterium atoms. A good fit to the data is obtained for β of 0.5 (Fig. 5c and Appendix). The same data were also plotted against the remaining fraction of hydrogen in the sample (Fig. 6c and Appendix). In this frame, the whole dataset can be satisfactorily described by a Rayleigh distillation equation:

$$\delta D = 1000 \cdot \left(F^{\left(\frac{1}{\alpha}-1\right)} - 1\right), \quad (7)$$

where F is the remaining fraction of hydrogen in the solid residue and α is the fractionation factor. This factor can describe either an equilibrium fractionation between coexisting H-bearing species, or a purely kinetic process. In the latter case, assuming that desorbed hydrogen molecules behave as an ideal gas, the fractionation factor should be close to $\sqrt{m_D/m_H} = 1.414$. Our best fit is obtained for α=1.46±0.04, which is in excellent agreement with the expected behavior of an ideal gas. These two different approaches therefore firmly suggest that the diffusion of protons and deuterons within the structure of grossular occurs at a rate that only depends on their masses. In other words and following

the description of the isotope effects of diffusion in crystalline solids, there is no significant interaction between the lattice vibrations of mineral and those of protons and deuterons.

4.4. Geochemical implications

The source of water in planetary bodies is investigated by measuring the D/H ratio because different regions of the solar system show very distinct D/H signatures (Hartogh et al., 2011; Altwegg et al., 2015). The hydrogen isotope fingerprint is thus a major proxy to study the provenance of water in bodies throughout the solar system, including Earth, the Moon, Mars, and the asteroid belt (e.g. Alexander et al. 2012; Saal et al. 2013; Sarafian et al., 2014; Hallis et al., 2015; Barnes et al., 2016). However, several episodes of hydration/dehydration/evaporation/degassing have affected these planetary bodies overtime (see for instance Saal et al., 2008 for the Moon). A reliable modeling of the isotopic modifications induced by the successive events that may have affected the measured samples is thus required to assess the origin of water in these bodies. Saal et al. (2013) measured the isotopic composition of water accommodated in lunar glasses and inclusions. They performed a detailed analysis of their data with a particular emphasis on the kinetic isotopic effect of dehydration. They considered the possible contribution of molecular water, hydroxyl and molecular hydrogen to this kinetic fractionation. An undisputable conclusion of their models is that the typical β-value for molecular hydrogen has to be lower than 0.06. Our experimental results collected on silica glasses are fully consistent with this conclusion (Fig. 6). This implies that as far as degassing of a melt is concerned the kinetic fractionation caused by degassing is very limited, at a few ‰ level and will be difficult to measure except if extensive distillation episodes are involved.

A drastically different conclusion is drawn when phases of interest are NAMs instead of glasses. In this case, the migration of protons through the crystalline network appears to be particularly efficient to separate D and H. To our knowledge no experiments have been carried out on other minerals of this family (e.g. olivines and pyroxenes). Concerning hydrous minerals, King et al., (2009) reported diffusion-driven D/H fractionation during the partial dehydration of an amphibole (kaersutite). They also observed marked isotopic profiles spatially correlated to water concentration profiles. These profiles were understood as the consequence of the diffusion of an interstitial species (protons/deuterons) and the

dataset is satisfactorily described by Eq. 4 with a β-value close to 0.5. Obviously, our results urge for the quantification of this β-coefficient for major upper mantle minerals (i.e. pyroxenes and olivines). Grossular and amphibole crystals, however, exhibit very comparable results, with $\beta \approx 0.5$. This suggests that β could also be very close to 0.5 for a large array of minerals. If so, the determination of the source reservoir of planetary water inferred from inclusions hosted in such minerals should be carefully corrected for the possible multi-stage hydration/dehydration (e.g. Hallis et al., 2015). If diffusion within the inclusion itself is probably inefficient to modify significantly the isotopic composition of dissolved water, the transport through the host mineral could modify this isotopic composition at the level of several 100‰.

5. Conclusion

Several experimental set-ups and silicate materials (glasses, melts, minerals) were used in order to mimic water-silicate interactions in different geo/cosmochemical environments and investigate associated H-isotope fractionation. Controlled hydration/dehydration experiments were performed. When molecular water is the mobile species (in hydrous phases and hydrated glasses and melts), no significant kinetic isotopic effect could be measured (within ±20‰); conversely when hydrogen is the dominant mobile species (i.e. in nominally anhydrous minerals) within the silicate framework, an extreme kinetic isotopic effect is observed. The geochemical and geophysical contexts (e.g. presence of water vapor vs. liquid; bubble degassing vs. hydration; diffusion in solids vs. diffusion in liquids, high vs. low pressure environments…) are not the dominant factors controlling the extent of the kinetically driven isotope fractionation. The speciation of water within the silicate and the microscopic mechanism involved in the diffusion process are, instead, the dominant factors. They may obviously be influenced by extrinsic intensive parameters, but is it essentially controlled by the crystal chemistry of the silicates of interest. Our results can thus probably be applied to a much broader range of geological and astrophysical environments provided that the cristallochemistry of 'water' accommodated into the minerals of interest are known.

Acknowledgment

This work was supported by the French ANR Program (2011JS56 004 01, FrIHIDDA) and by the Region Nord-Pas de Calais to M.R. The FTIR apparatus are supported by the Chevreul Institute, the Conseil Regional de Nord-Pas de Calais, the ERDF, and the Institut National des Sciences de l'Univers (INSU, CNRS).

Figure captions:

Figure 1: a) Hydroxyl concentration profiles measured by FTIR after the partial hydration of nominally water-poor (8 ppm) silica samples at 1000°C. b) Associated δD relative to the mean isotopic composition of the inner part of the sample and measured by SIMS. The grey bar represent the typical 1sd error envelop.

Figure 2: a) Hydroxyl concentration profiles measured by FTIR after the partial dehydration of nominally water-rich (~150 ppm) silica samples at 1000°C. b) Associated δD relative to the mean isotopic composition of the inner part of the sample and measured by SIMS. The grey bar represent the typical 1sd error envelop.

Figure 3: a) Hydroxyl concentration profiles measured around bubbles formed by magma decompression in a rhyolitic melt (data measured by SIMS and normalized to the initial water concentration measured far from the bubbles, see text for more details. b) Associated δD relative to the mean isotopic composition measured by SIMS far from the bubbles. The grey bar represent the typical 1sd error envelop.

Figure 4: Transmission μ-FTIR spectra (in the region 3000-4000 cm^{-1}) collected across the grossular sample after hydrogen extraction experiment. The spectra exhibiting large absorptions were collected at the center of the sample.

Figure 5: a) Hydroxyl concentration profiles measured across a grossular single crystal after partial water extraction (Data measured by SIMS and FTIR and normalized to the initial water content measured at the center of the sample, see text for more details). b) Associated raw D/H measured by SIMS along 4 different profiles and collected during different analytical sessions. These data are given without matrix effect corrections against VSMOW. The best linear fit to the data collected at the center of the sample is also shown (see text for more details). c) D/H measured along hydroxyl concentration profiles internally corrected for matrix effect based on the linear fit shown on panel b (see text for more details). The fit to the data presented here is for β=0.5.

Figure 6: Models for D/H redistibution during diffusion at 1000°C of water molecules and protons in a silica glass after a) 8 days and b) 30 days (see text for more details). c) Rayleigh distillation plot describing the D/H redistibution during water extraction from a grossular single crystal.

Appendix:

In this appendix, we present fit to the raw isotopic data (spatially resolved in panel a and Rayleigh distillation plot of the same dataset on panel b) measured across a grossular single crystal after partial water extraction. These figures are the counterparts of Fig. 5c and Fig. 6c respectively. The presented data here were not processed. Instead, the data set was only internally standardized for the instrumental mass fractionation, considering the average isotopic composition of the inner part of the sample as the mean isotopic composition of the bulk starting grossular crystal (see text for the precise definition of *the inner part* of the sample). Fit to the data are identical to those presented in Fig. 5c and 6c. It is thus clear that the baseline correction improves the visual quality of the fit to the data but does not change the parameters of the best fit nor the conclusions of the article concerning the extent of the fractionation induced by partial water extraction from nominally anhydrous minerals.

References:

Abreu N. M. and Brearley A. J. (2010) Early solar system processes recorded in the matrices of two highly pristine CR3 carbonaceous chondrites, MET00426 and QUE99177. Geochim. Cosmochim. Acta 74, 1146–1171.

Albarède F. (2009) Volatile accretion history of the terrestrial planets and dynamic implications. Nature 7268, 1227-1233.

Altwegg, K. et al. (2015) 67P/Churyumov-Gerasimenko, a Jupiter family comet with a high D/H ratio. Science 347, 3–6.

Barnes J.J., Kring D.A., Tartèse R., Franchi I.A., Anand M. and Russel S.S. (2016) An asteroidal origin for water in the Moon. Nat. Com., 7, 11684.

Behrens H. (2010) Ar, CO_2 and H_2O diffusion in silica glasses at 2 kbar pressure. Chemical Geology 272 (1–4), 40–48.

Behrens H., Zhang Y. and Xu Z. (2004) H_2O diffusion in dacitic and andesitic melts. Geochimica et Cosmochimica Acta 68, 5139–5150.

Blanchard M. and Ingrin J. (2004) Kinetics of deuteration in pyrope. European Journal of Mineralogy, 16, 567-576.

Bose K. and Ganguly J. (1995) Quartz–coesite transition revisited: reversed experimental determination at 500–1200°C and retrieved thermochemical properties. Am. Mineral. 80, 231–238.

Cohen-Addad C., Ducros P. and Bertaut E.F. (1967) Etude de la substitution du groupement SiO_4 par $(OH)_4$ dans les composés $Al_2Ca_3(OH)_{12}$ et $Al_2Ca_3(SiO_4)_{2.16}(OH)_{3.36}$ de type grenat. Acta Crystallographica, 23, 220- 230.

Davis K.M. and Tomozawa M. (1996) An infrared spectroscopic study of water-related species in silica glass. J. Non-Cryst. Solids 201, 177-198.

Davis K.M., Agarwal A., Tomozawa M. and Hirao, K. (1996) Quantitative infrared spectroscopic measurement of hydroxyl concentrations in silica glass. J. Non-Cryst. Solids 203, 27–36.

Demouchy S. and Mackwell S. (2003) Water Diffusion in Synthetic Iron-Free Forsterite. Phys. Chem. Minerals. 30. 786-794.

Dingwell D. B. and Webb S. L. (1990) Relaxation in silicate melts. Eur. J. Mineral. 2, 427–449.

Doremus R.H. (1995) Diffusion of water in silica glass. J. Mater. Res. 10, 2379-2389.

Doremus R.H. (1969) in : J.W. Michell, R.C. DeVries, R.W. Roberts, P. Cannon (Eds.), Reactivity in solids, Wiley, New York, 667.

Drake M.J. (2005) Origin of water in terrestrial planets. Meteoritics and planetary science 40, 519-527.

Fanara S., Behrens H. and Zhang Y. (2013) Water diffusion in potassium-rich phonolitic and trachytic melts. Chemical Geology, 346, 149-161.

Hallis L.J., Huss G.R., Nagashima K., Taylor G.J., Halldórsson S.A., Hilton D.R., Mottl M.J. and Meech K.J. (2015) Evidence for primordial water in Earth's deep mantle. Science 350, 6262 (2015).

Hamada M., Laporte D., Cluzel N., Koga K.T. and Kawamoto T. (2010) Simulating bubble number density of rhyolitic pumices from Plinian eruptions: constraints from fast decompression experiments. Bulletin of Volcanology, 72: 735-746.

Hartogh P., Lis D.C., Bockelée-Morvan D., de Val-Borro M., Biver N., Küppers M., Emprechtinger M., Bergin E. A., Crovisier J., Rengel M., Moreno R., Szutowicz S. and Blake G. A. (2011) Ocean-like water in the Jupiter-family comet 103P/ Hartley 2. Nature 478, 218–220.

Hauri E. H., Saal A. E., Rutherford M. J. and Van Orman J. A. (2015) Water in the Moon's interior: Truth and consequences. Earth Planet. Sci. Lett. 409, 252–264.

Hercule S. and Ingrin J. (1999) Hydrogen in diopside: Diffusion, kinetics of extraction-incorporation, and solubility. American Mineralogist, 84, 1577- 1587.

Horita J. and Wesolowski D.J. (1994) Liquid-vapor fractionation of oxygen and hydrogen isotopes of water from the freezing to the critical temperature. Geochim. Cosmochim. Acta, 58, 3425-3437.

Hui H., Zhang Y., Xu Z. and Behrens H. (2008) Pressure dependence of the speciation of dissolved water in rhyolitic melts. Geochim. Cosmochim. Acta, 72, 3229-3240.

Ihinger P. D., Zhang Y. and Stolper E. M. (1999) The speciation of dissolved water in rhyolitic melt. Geochim. Cosmochim. Acta 63, 3567–3578.

Ingrin J. and Blanchard M. (2006) Diffusion of Hydrogen in Minerals. *Review in Mineralogy & Geochemistry.* 62, 291-320.

Jochum et al., (2006) MPI-DING reference glasses for in situ microanalysis: New reference values for element concentrations and isotope ratios. Geochem. Geophys. Geosys. 7, Q02008.

King P.L., Guan Y., Vennemann T.W., Leshin L.A. and Sharp Z.D.(2009) The role of dehydrogenation on the hydrogen contents and dD of kaersutites. LPSC Conference #2322

Kohlstedt D.L. and Mackwell S.J. (1998) Diffusion of hydrogen and intrinsic point defects in

olivine. Zeitschrift für Physikalische Chemie, 207, 147-162.

Kurka A., Blanchard M. and Ingrin J. (2005) Kinetics of hydrogen extraction and deuteration in grossular. Min. Mag. 69, 359-371.

LeClaire A. D. (1966) Some comments on the mass effect in diffusion. Philos. Mag. 14, 1271–1284.

Lunine J.I., Chambers J., Morbidelli A. and Leshin L.A. (2003) The origin of water on Mars, Icarus, 165, 1- 8.

Mackwell S.J. and Kohlstedt D.L. (1990) Diffusion of Hydrogen in Olivine: Implications for Water in the Mantle. Journal of Geophysical Research 95, 5079-5088.

Maldener J., Hösch A., Langer K. and Rauch F. (2003) Hydrogen in some natural garnets studied by nuclear reaction analysis and vibrational spectroscopy. Physics and Chemistry of Minererals, 30, 337-344.

Moulson A.J. and Roberts J.P. (1960) Water in silica glass. Trans. Br. Ceram. Soc. 59, 388.

Mourtada-Bonnefoi C.C. and Laporte d. (2004) Kinetics of bubble nucleation in a rhyolitic melt: an experimental study of the effect of ascent rate. Earth. Planet. Sci. Let. 218, 521-537.

Tamic N., Behrens H. and Holtz F. (2001) The solubility of H_2O and CO_2 in rhyolitic melts in equilibrium with a mixed CO_2/H_2O fluid phase, Chem. Geol. 174, 333-347

Ni H., Xu Z. and Zhang Y. (2013) Hydroxyl and molecular H2O in a haploandesitic melt. Geochimica et Cosmochimica Acta 103, 36-48.

Oeser M., Dohmen R., Horn I., Schuth S. and Weyer S. (2015) Processes and time scales of magmatic evolution as revealed by Fe-Mg chemical and isotopic zoning in natural olivines. Geochimica et Cosmochimica Acta, 154, 130-150.

Pilorgé, H., Reynard, B., Remusat, L., Le Floch, S., Montagnac, G. and Cardon, H. (2017) D/H diffusion in serpentine. Geochim. Cosmochim. Acta 211, 355-372.

Prinn R.G. and Fegley B., Jr. (1989) Origin and Evolution of Planetary and Satellite Atmospheres, Vol. 1 (Tucson, AZ: University of Arizona Press)

Richter F.M., Liang Y. and Davis A.M. (1999) Isotope fractionation by diffusion in molten silicates. Geochimica et Cosmochimica Acta 63, 2853-2861.

Richter F., Chaussidon M., Mendybaev R. and Kite E. (2016) Reassessing the cooling rate and geologic setting of Martian meteorites MIL 03346 and NWA 817. GCA 182 1-23.

Roskosz, M., Luais, B., Watson, H.C., Toplis, M.J., Alexander, C.M.O.D., Mysen, B.O., 2006. Experimental quantification of the fractionation of Fe isotopes during metal segregation from a silicate melt. Earth and Planetary Science Letters 248, 851-867.

Roskosz M. Laurent B., Leroux H. and Remusat L. (2016) Experimental investigation of irradiation-driven hydrogen isotope fractionation in analogues of protoplanetary hydrous silicate dust. Astrophys. J. 832, 55.

Rossman G.R and Aines R.D. (1991) The hydrous components in garnets: grossular-hydrogrossular. American Mineralogist, 76, 1153-1164.

Saal A.E., Hauri E.H., Van Orman J.A. and Rutherford M.J. (2013) Hydrogen isotopes in lunar volcanic glasses and melt inclusions reveal a carbonaceous chondrite heritage. Science 340, 1317–1320.

Saal A.E., Hauri E.H., Cascio M.J., Van Orman J. A. and Rutherford M. J. and Cooper R.F. (2008) Volatile content of lunar volcanic glasses and the presence of water in the Moon's interior, Nature, 454, 192-195.

Sarafian A.R., Nielsen S.G., Marschall H.R., McCubbin F.M. and Monteleone B.D. (2014) Early accretion of water in the inner solar system from a carbonaceous chondrite-like source. Science 346, 623–626.

Schmidt B.C., Blum-Oeste N. and Flagmeier J. (2013) Water diffusion in phonolite melts. Geochim. Cosmochim. Acta 107, 220-230.

Schoen A. H. (1958) Correlation and the isotope effect for diffusion in crystalline solids. Phys. Rev. Lett. 1, 138–140.

Sio C.K.I., Dauphas N., Teng F.-Z., Chaussidon M., Helz R.T. and Roskosz M. (2013) Discerning crystal growth from diffusion profiles in zoned olivine by in situ Mg–Fe isotopic analyses. Geochim. Cosmochim. Acta 123, 302–321.

Stolper E.M. (1982a) The speciation of water in silicate melts. Geochim. Cosmochim. Acta 46, 2609–2620.

Tartèse R., Anand M., Barnes J.J., Starkey N.A., Franchi I.A. and Sano Y. (2013) The abundance, distribution, and isotopic composition of hydrogen in the Moon as revealed by basaltic lunar samples: Implications for the volatile inventory of the Moon. Geochim. Cosmochim. Acta 122, 58–74.

Tharmalingam K. and Lidiard A. B. (1959) Isotope effect in vacancy diffusion. Philos. Mag. 4, 899–906.

Tomozawa M. and Davis K.M. (1999) Time dependent diffusion coefficient of water into silica glass at low temperature. Mat. Sci. Eng. A272, 114-119.

Van Orman J.A. and Krawczynski M.J. (2015) theoretical constraints on the isotope effect for diffusion in minerals. Geochim. Cosmochim. Acta 164, 365-381.

Woods S.C., Mackwell S. and Dyar D. (2000) Hydrogen in diopside: Diffusion profiles. American Mineralogist, 85, 480-487

Zhang P., Ingrin J., Depecker C. and Xia Q-K. (2015) Kinetics of deuteration in andradite. *Amer. Min.* 100, 1400-1410.

Zhang Y. (1999) H_2O in rhyolitic glasses and melts: measurement, speciation, solubility, and diffusion, Rev. Geophys. 37, 493-516.

Zhang Y., Jenkins J. and Xu Z. (1997) Kinetics of the reaction $H_2O+O=2OH$ in rhyolitic glasses upon cooling : geospeedometry and comparison with glass transition. Geochim. Cosmochim. Acta 61, 2167.

Zhang Y. and Ni H. (2010) Diffusion of H, C, and O components in silicate melts. *In* Diffusion in Minerals and Melts. Reviews in Mineralogy and Geochemistry, vol. 72 (eds. Y. Zhang and D. J. Cherniak). Mineral. Soc. Am., Washington, DC, pp. 171–225.

Zhang Y., Stolper E.M. and Ihinger P.D. (1995) Kinetics of the reaction H2O+O=2OH in rhyolitic and albitic glasses: preliminary results. American Mineralogist 80, 593–612.

Table 1: Hydroxyl concentration profiles measured after the partial hydration of nominally water-poor (8 ppm) silica samples, and the partial dehydration of nominally water-rich (~150 ppm) silica samples at 1000°C.

Hydration at 1000°C. Hydroxyl concentration (in ppm)				Dehydration at 1000°C. Hydroxyl concentration (in ppm)		
Distance (μm)	30 days	8 days	3 days	Distance (μm)	Starting material	3 hours
0	136	132	160	0	0	0
10	135	130	148	20	1	1
20	133	120	132	40	6	1
30	135	110	110	60	19	1
40	134	101	88	80	22	1
50	132	94	64	100	28	5
60	127	83	39	120	43	5
70	121	75	25	140	42	10
80	114	68	16	160	55	12
90	107	60	13	180	61	11
100	100	52	11	200	64	13
110	94	44	10	220	66	17
120	87	37	9	240	66	19
130	82	30	9	260	67	19
140	76	24	9	280	65	19
150	70	17	9	300	66	20
160	64	12	9	320	66	19
170	57	9	9	340	66	20
180	52	7	10	360	68	20
190	47	7	9	380	67	20
200	41	8	9	400	66	22
210	36	8	9	420	67	21
220	30	9	9	440	67	22
230	25	9	9	460	67	21
240	20	9	9	480	67	22
250	15	9	9	500	68	22
260	13	8	9	520	67	22
270	10	8	8	540	68	22
280	7	8	9	560	72	22
290	7	8	9	580	67	22
300	8	8	9	600	71	23
310	8	8	8	620	68	23
320	9	8	8	640	67	23
330	9	9	8	660	67	22
340	9	8	9	680	67	23
350	10	9	10	700	67	23
360	10	10	11	720	69	23
370	11	11	12	740	73	22
380	10	11	11	760	69	23
390	10	11	10	780	68	23
400	10	11	10	800	68	23
410	10	12	9	820	68	23
420	10	11	11	840	68	23
430	10	10	11	860	71	23
440	10	9	12	880	71	23
450	9	11	12	900	69	23
460	9	10	10	920	68	22
470	9	10	10	940	71	23
480	8	10	9	960	71	23
490	8	8	8	980	73	23
				1000	67	23
				1020	71	24
				1040	67	25
				1060	68	25
				1080	71	24
				1110	67	22
				1120	70	23

				1140	65	23
				1160	70	24
				1180	65	24
				1200	68	22
				1220	69	23
				1240	69	23
				1260	70	22
				1280	70	22
				1300	68	22
				1320	68	22
				1340	69	21
				1360	68	22
				1380	67	21
				1400	68	21
				1420	67	20
				1440	66	21
				1460	65	21
				1480	66	20
				1500	66	20
				1520	66	20
				1540	64	20
				1560	64	17
				1580	66	17
				1600	64	17
				1620	64	16
				1640	63	5
				1660	63	3
				1680	62	3
				1700	65	4
				1720	68	3
				1740	68	1
				1760	9	0
				1780	6	0
				1800	3	0
				1820	0	0

Table 2: Hydrogen isotope compositions of partially hydrated/dehydrated silica glasses. Isotopic compositions are given relative to the composition of the inner part of the sample (unaffected by diffusive processes) or to the isotopic composition of the starting material (see text for more information).

Hydration at 1000°C. δD (‰. 1 s.d.)								**Dehydration at 1000°C. δD (‰. 1 s.d.)**			
Distance (µm)	**30 days**			**Distance**	**8 days**			**Distance (µm)**	**3 hours**		
45	-32	±	24	42	-58	±	23	30	-5	±	25
69	-12	±	24	66	-41	±	27	55	-31	±	26
94	-11	±	28	90	0	±	31	80	-34	±	24
119	1	±	24	113	-59	±	36	105	-63	±	27
144	62	±	24	137	9	±	38	129	-36	±	28
169	-3	±	23	161	46	±	42	154	-54	±	23
194	-35	±	28	185	11	±	39	179	-42	±	22
219	-22	±	30	209	-17	±	42	204	2	±	23
243	-58	±	27	233	-60	±	33	229	2	±	22
268	16	±	27	257	47	±	35	254	-1	±	27
293	-32	±	31	281	-46	±	26	279	1	±	21
318	-13	±	33	305	27	±	42	303	-38	±	25
343	72	±	35	329	45	±	32	328	-30	±	24
368	-1	±	33	352	48	±	36	353	-4	±	26
392	-7	±	31	376	7	±	33				
417	-1	±	37	400	34	±	46				
442	-14	±	35	424	31	±	38				
467	22	±	45	448	-41	±	37				
492	28	±	41	472	18	±	61				
517	39	±	29								

Table 3: Hydrogen concentration and isotope composition profiles measured by SIMS around bubbles formed by magma decompression in a rhyolitic melt (H/Si data are normalized to the initial water concentration measured far from the bubbles, see text for more details).

Normalized H/Si concentration profiles		
Sample	Distance (µm)	H/Si (normalized)
167 kPa/s to 70 Mpa	25	0.87
	56	0.88
	89	0.93
	128	0.94
	163	1.00
	194	1.01
	226	1.01
	258	0.99
	285	0.99
27.8 kPa/s to 85 Mpa	25	0.68
	55	0.79
	87	0.85
	120	0.90
	158	0.95
	192	0.98
	228	0.99
	264	1.02
	301	0.99
27.8 kPa/s to 88 Mpa	25	0.94
	53	0.96
	90	0.96
	130	0.97
	177	1.00
	215	1.00
	249	1.00
	285	1.00

Hydrogen isotopic compositions												
27.8 kPa/s to 85 Mpa				27.8 kPa/s to 88 Mpa				167 kPa/s to 70 Mpa				
Distance (µm)	δD (‰. 1 s.d.)			Distance (µm)	δD (‰. 1 s.d.)			Distance (µm)	δD (‰. 1 s.d.)			
368	-9	±	3	757	-15	±	6	25	5	±	6	
337	-16	±	4	479	-41	±	6	55	16	±	6	
306	-9	±	5	465	18	±	4	85	-8	±	6	
280	0	±	3	450	-13	±	6	115	-3	±	6	
257	2	±	5	425	-4	±	7	145	2	±	5	
228	-3	±	4	473	28	±	5	175	-3	±	5	
206	-17	±	5	434	23	±	5	205	-10	±	5	
186	33	±	4	425	23	±	6	25	29	±	6	
128	7	±	5	253	-37	±	7	45	-4	±	8	
73	12	±	8	25	-34	±	6	70	2	±	8	
111	-28	±	15	59	2	±	7	89	9	±	8	
147	1	±	18	83	32	±	6	114	1	±	7	
80	15	±	18	107	35	±	7	134	-6	±	7	
52	1	±	10	132	30	±	5	159	-8	±	7	
26	10	±	18	157	25	±	6	179	-9	±	7	
20	1	±	15	182	15	±	3	204	-7	±	9	
20	17	±	16	206	-4	±	4	224	-6	±	8	
50	-23	±	8	231	-14	±	3	25	-30	±	7	
80	-11	±	11	256	4	±	3	53	-8	±	8	
110	23	±	8	281	-8	±	4	84	8	±	6	
140	-13	±	11	306	-8	±	3	111	4	±	5	
20	7	±	17	30	-26	±	4	141	3	±	9	
				55	12	±	4	168	9	±	7	
				80	1	±	3	198	5	±	9	
				105	-3	±	3	232	-3	±	6	
				317	3	±	3	261	13	±	7	
				314	0	±	2					
				38	-10	±	4					
				63	-9	±	2					
				269	31	±	3					
				113	30	±	4					
				138	26	±	4					
				25	-1	±	3					
				49	-11	±	10					
				75	-8	±	9					
				101	-5	±	11					
				125	-32	±	13					
				149	-18	±	12					
				175	-17	±	11					
				201	-18	±	11					

Table 4: Hydroxyl concentration profiles measured across the grossular single crystal after partial water extraction (Data measured by SIMS and FTIR). They are normalized to the initial water content measured at the center of the sample, see text for more details). Associated hydrogen isotope compositions (relative to VSMOW and without matrix effect correction) measured by SIMS along 4 different profiles and collected during different analytical sessions.

Normalized hydroxyl concentration profiles					Hydrogen isotope compositions (‰. 1 s.d.)				
Distance µm	FTIR (60 µm)	FTIR (30 µm)	OH/Si (SIMS)	OH/O (SIMS)	Distance µm	Profil #1	Profil #2	Profil #3	Profil #4
20	48				3		363 ± 40		
25			68	67	3			321 ± 49	
30		34			23		513 ± 14		
50			69	68	23			510 ± 20	
60	60	48			43		451 ± 10		
75			75	72	43			479 ± 13	
90		60			63		290 ± 14		
100	70				63			320 ± 7	
100			82	81	73		233 ± 10		
120		68			73			245 ± 11	
125			85	82	93		108 ± 11		
140	79				93			131 ± 8	
150		74			113		75 ± 15		
150			88	89	113			105 ± 10	
175			90	88	133		20 ± 17		
180	86	77			133			51 ± 11	
200			92	91	153		-1 ± 16		
210		82			153			24 ± 14	
220	91				173		14 ± 11		
240		86			173			36 ± 12	
250			94	93	193		-16 ± 15		
260	94				193			8 ± 14	
270		90			213		-11 ± 10		
300	96	93			213			-7 ± 8	
300			98	96	228	23 ± 13			
330		95			233		7 ± 14		
340	97				253	28 ± 7			
350			98	97	253		-1 ± 10		
360		97			273		-12 ± 12		
380	98				275	3 ± 7			
390		98			300	-2 ± 7			
400			99	98	323		-22 ± 12		
420	99	99			325	-32 ± 9			
450		100			350	25 ± 7			
450			100	99	373		-13 ± 11		
460	100				375	-1 ± 7			
500	100				400	-12 ± 5			
500			100	100	423		-15 ± 6		
540	100				425	-12 ± 7			
550			99	98	450	-12 ± 5			
580	100				473		3 ± 8		
600			99	99	475	20 ± 5			
620	100				500	-13 ± 5			
650			98	99	523		-22 ± 7		
660	100				525	-23 ± 6			
700	99				550	8 ± 7			
700			97	98	573		5 ± 7		
740	99				575	-23 ± 5			
750			96	96	600	-7 ± 5			
775			94	91	623				-13 ± 6
780	98				625	-7 ± 5			
800			93	91	650	2 ± 6			
820	96				673				-7 ± 5
825			91	89	675	-8 ± 10			
850			91	91	700	19 ± 5			
860	92				723				11 ± 7
875			86	85	725	-4 ± 8			
900	88				750	6 ± 6			
900			85	84	773				8 ± 5
925			82	79	775	-13 ± 6			
940	80				800	12 ± 5			
950			79	75	823				-3 ± 4
975			71	67	825	4 ± 6			
980	71				850	15 ± 5			
1000			67	61	873				24 ± 5
1020	66				875	5 ± 7			
1025			68	60	923				58 ± 6
1060	50				973				68 ± 6
					1023				94 ± 7
					1063				534 ± 11

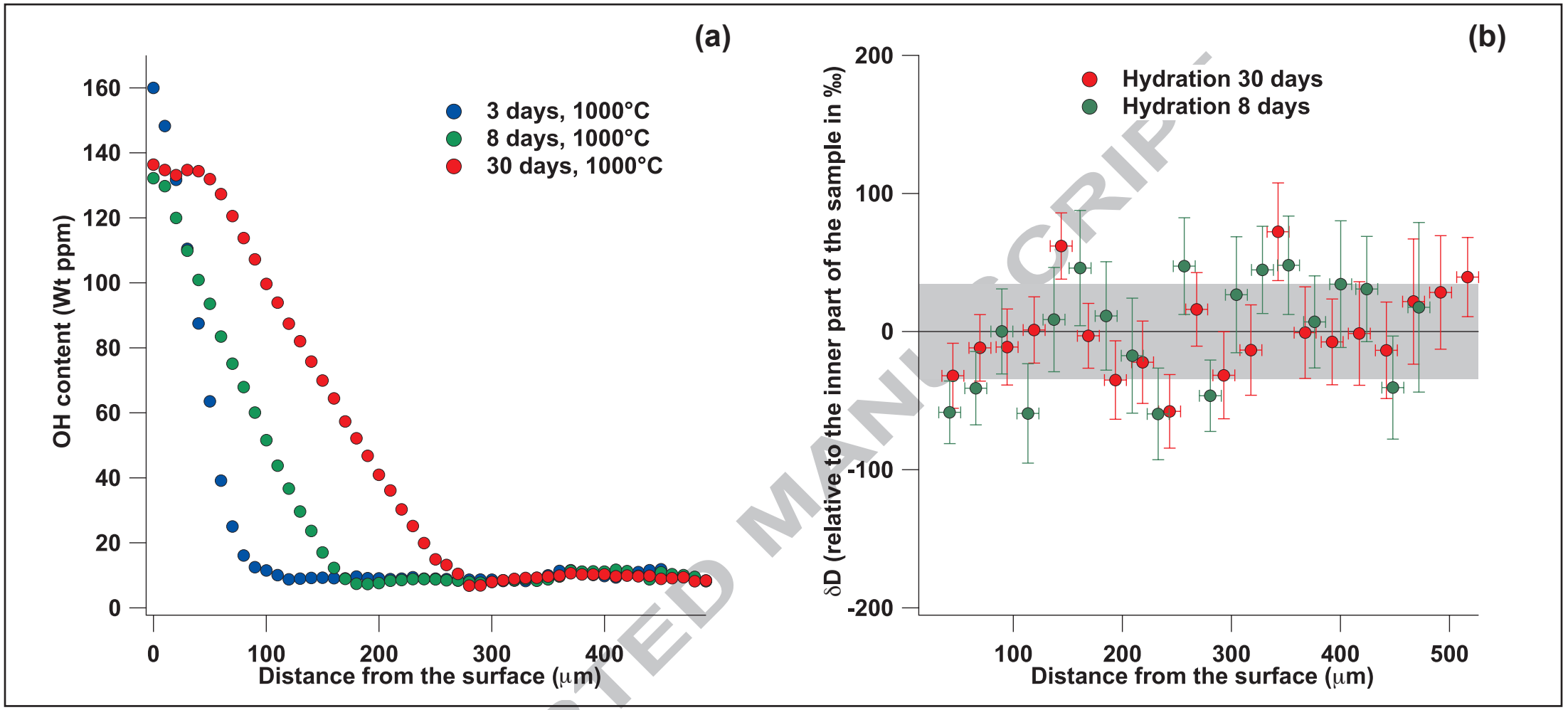

Figure 1

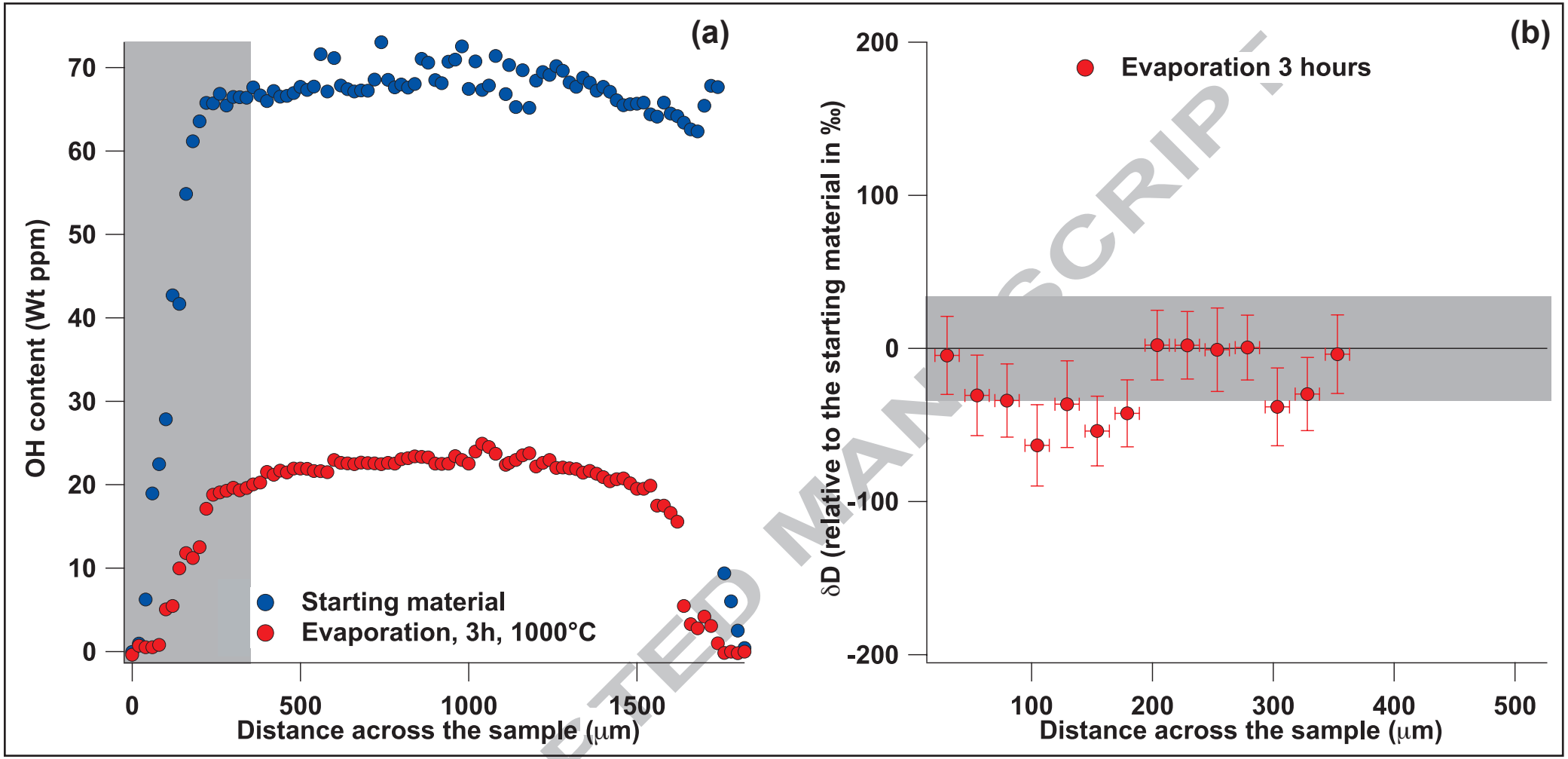

Figure 2

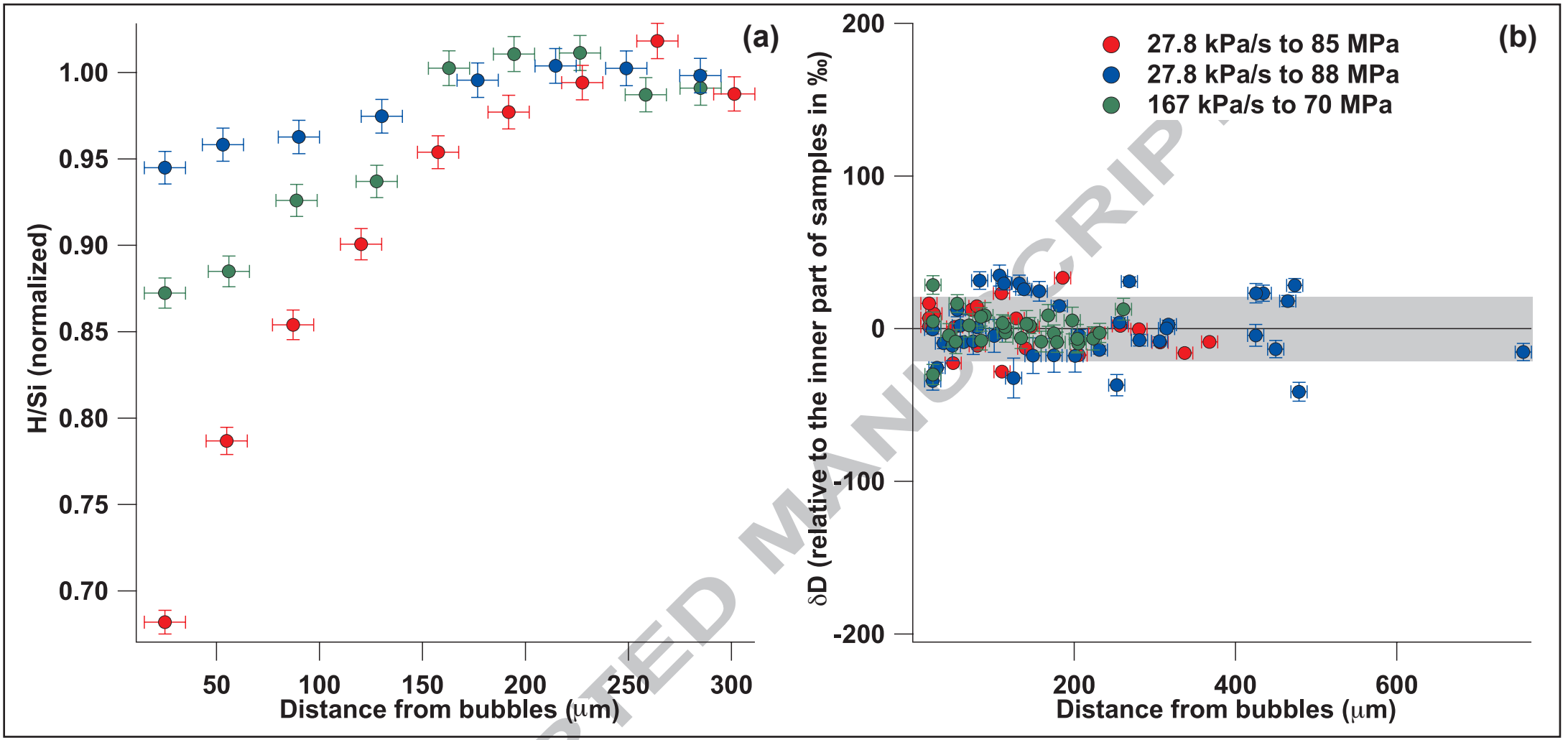

Figure 3

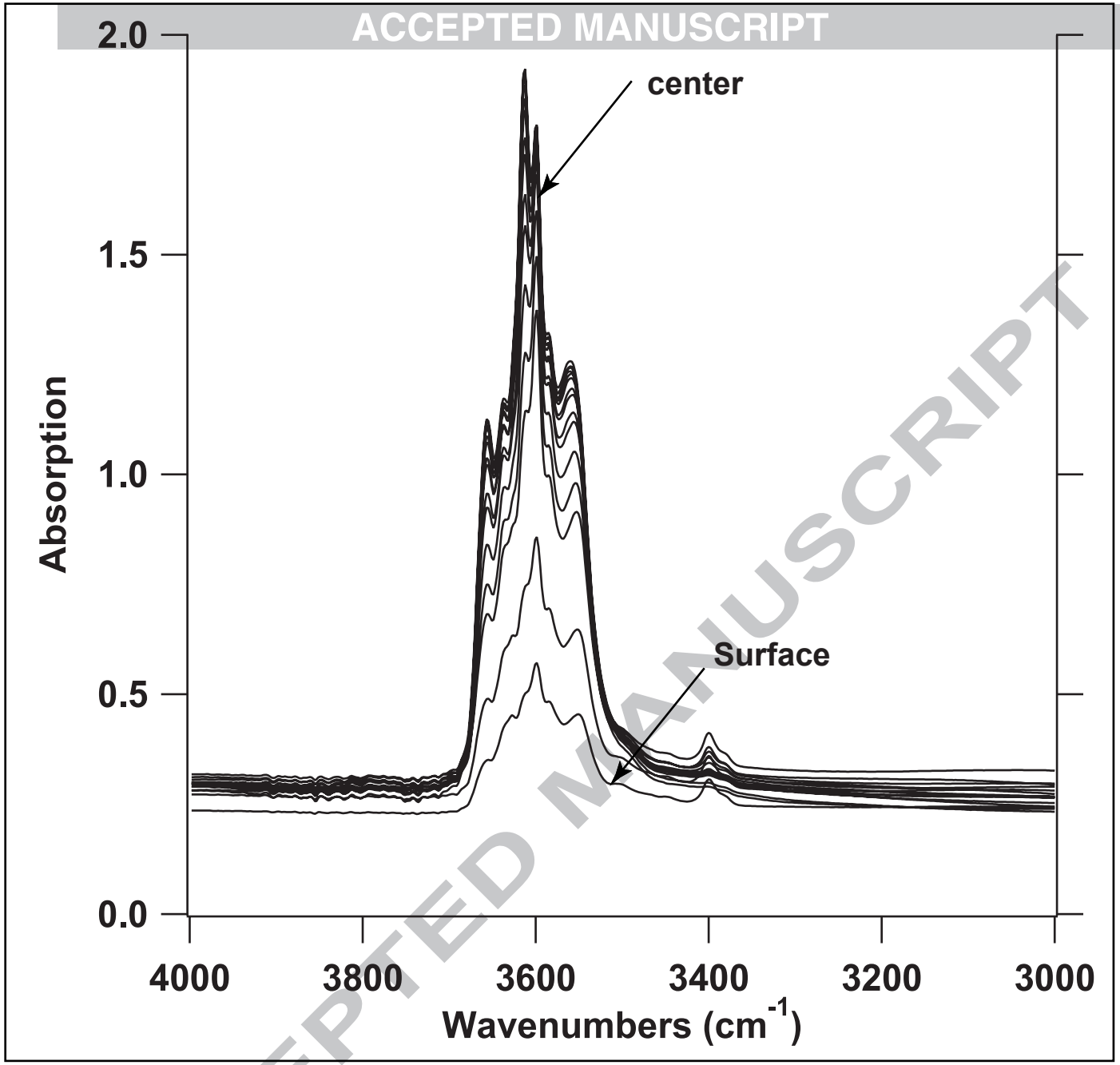

Figure 4

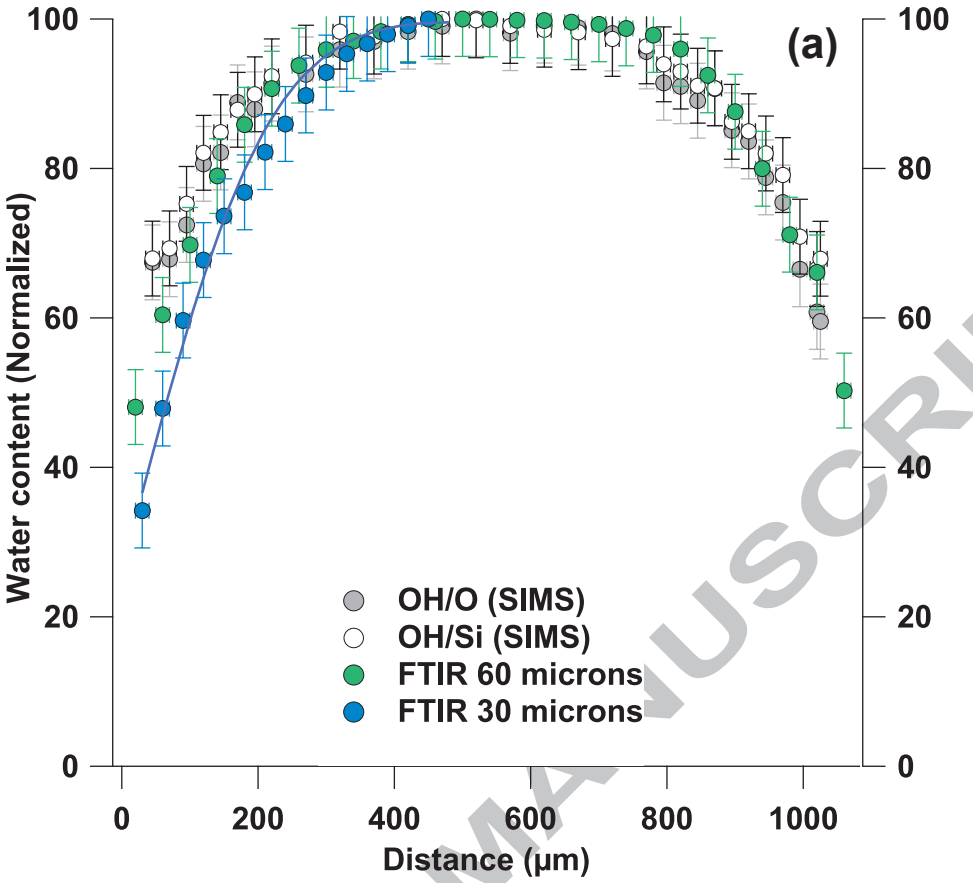

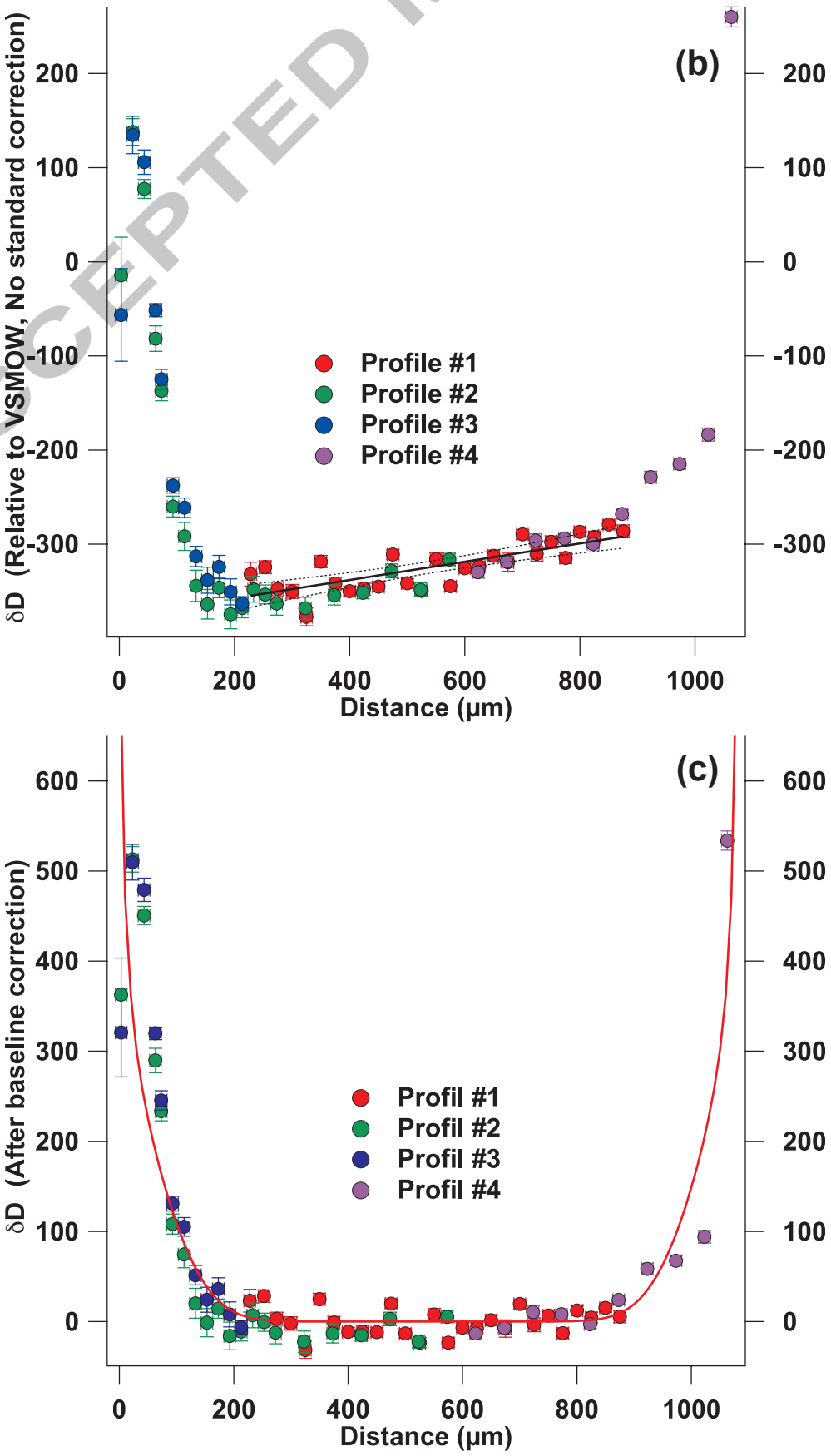

Figure 5

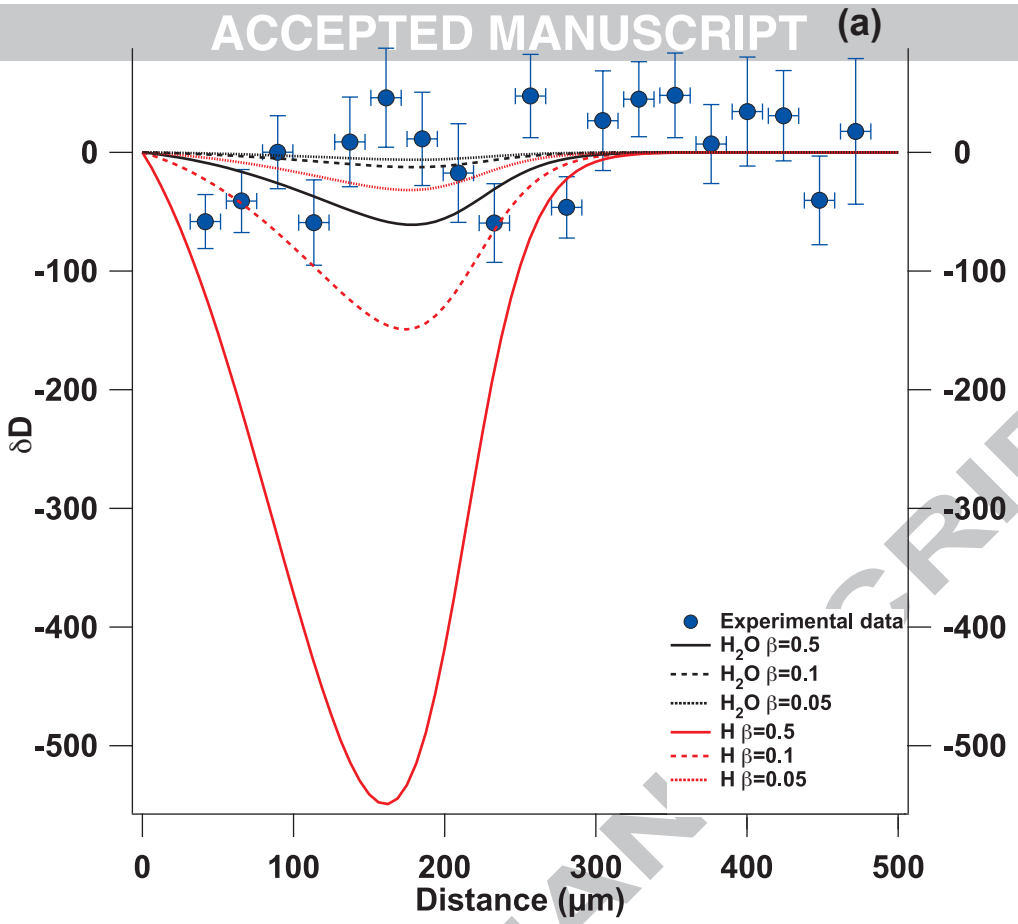

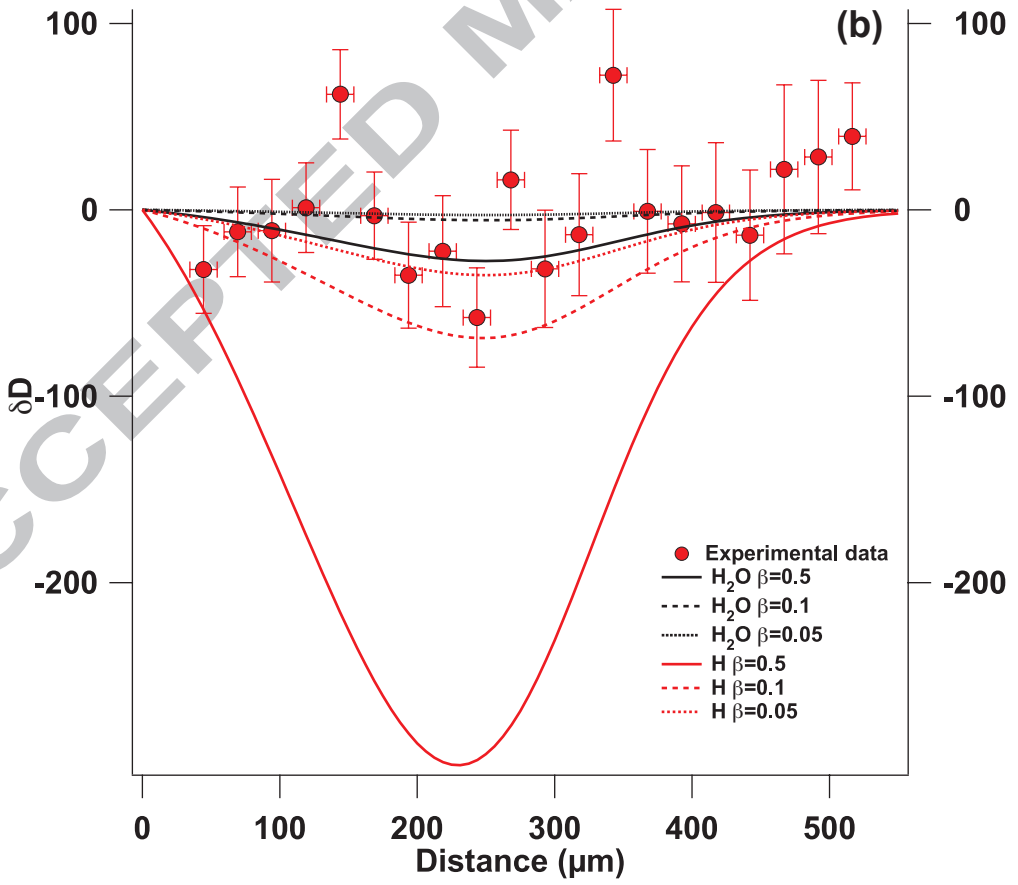

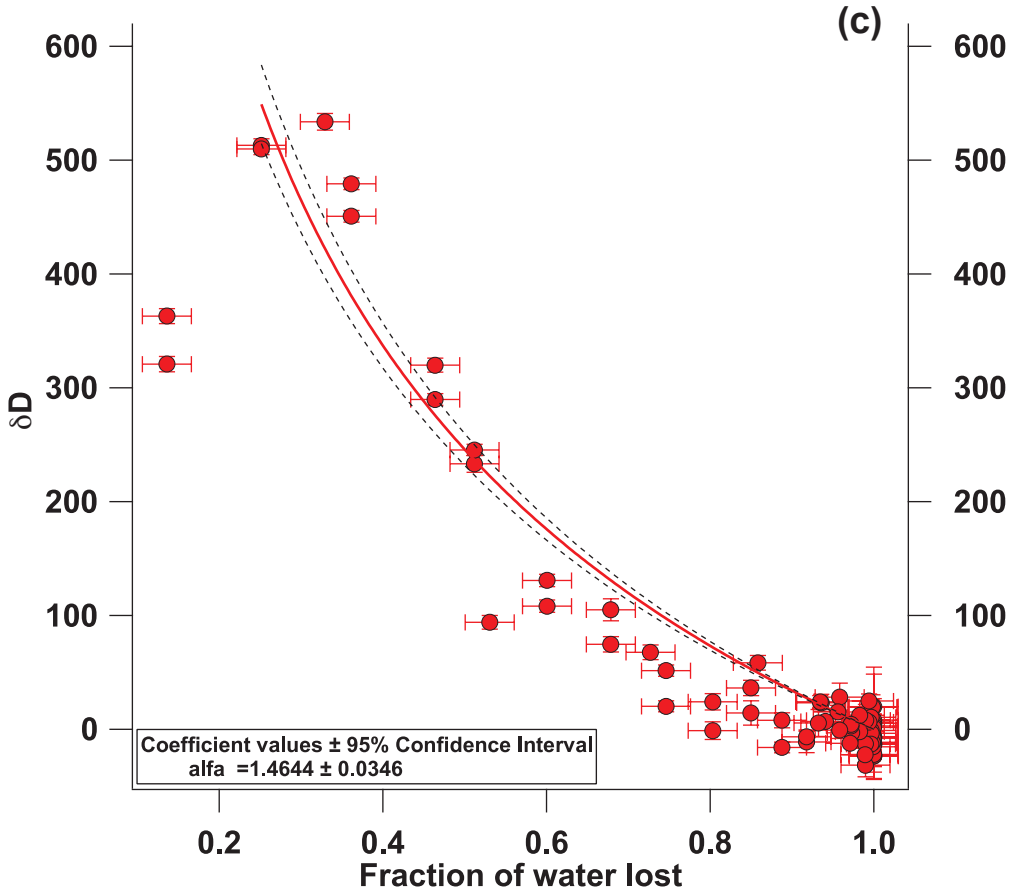

Figure 6

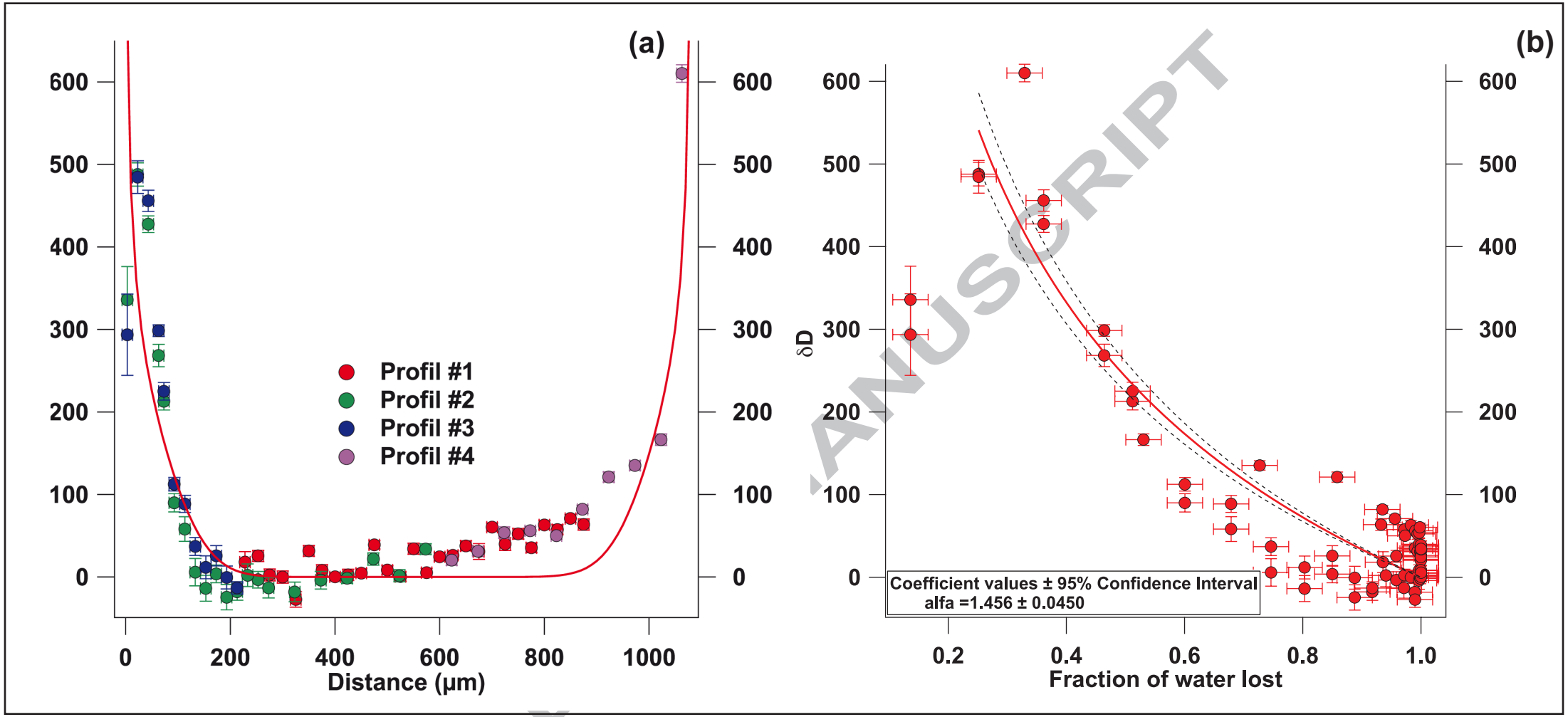

Fig. ANNEXE